大湾区显微科学与技术研究中心

Bay Area Center for Electron Microscopy

简讯

第13期

松山湖材料实验室
广东省东莞市大朗镇屏东路333号
Email: bacem@sslab.org.cn

出版日期：2025年8月1日

2025年第2期（总第13期）

耿皖荣副研究员受聘中国电子显微学会青年学者专家委员会委员和《电子显微学报》期刊青年编委

2025 年 2 月 8 日，中国电子显微镜学会(对外）第十一届常务理事会第四次扩大会议在海南陵水召开。会上，中国电子显微镜学会（对外）青年学者专家委员会正式成立，并在同期举办了第一届青年学者论坛。经电镜学会常务理事会商议决定，青年学者专家委员会由来自材料科学、生命科学、植物和生物医学等领域的 45 位青年科学家代表组成。大湾区显微科学与技术研究中心耿皖荣副研究员被聘为首届青年学者专家委员会委员（任期四年）和《电子显微学报》期刊的青年编委。

耿皖荣副研究员受聘《Interdisciplinary Materials》期刊学术编辑

2025 年 3 月，大湾区显微科学与技术研究中心耿皖荣副研究员被聘为 Interdisciplinary Materials（交叉学科材料）期刊的学术编辑，任期两年。

材料与其它学科的交叉是世界材料科技发展的前沿方向，是我国近年来倡导和重视的关键领域。Interdisciplinary Materials 期刊由武汉理工大学与 Wiley 集团联合出版，是国际上聚焦交叉学科材料前沿领域的首本高水平学术期刊，于 2022 年 1 月出版创刊号，9 月入选“中国科技期刊卓越行动计划高起点新刊”，2024 年 3 月获得国家新闻出版署颁发的期刊出版许可证，2024 年 6 月获得首个影响因子 24.5，在所属的 3 个细分领域中全部进入全球前 5%，位列 Q1 分区。该期刊主编为张清杰院士和傅正义院士，编委会包括国际杰出学者 30 人、两院院士 45 人，百余位国家高层次领军和青年人才担任期刊学术编辑。

大湾区电镜中心近期博士后岗位招聘方向

1、4D-STEM 技术与应用

建立基于 4D STEM 的电子叠层衍射 (electron ptychography) 的实验流程、参数及数据分析算法；开展叠层衍射重构的低电子束剂量、高空间分辨率成像与算法研究。

2、三维原子断层成像技术与应用 (3D AET)

构建基于三维原子成像技术和算法的实验平台，发展数据采集、存储、算法的新方法。结合像差校正透射电镜和聚焦离子束系统开展适用于块体样品的原子级电子断层成像实验技术与算法研究；基于原子级电子断层成像技术开展界面、新型极化拓扑畴等复杂结构的原子尺度三维结构与功能特性解析研究。

3、叠层衍射式电子断层成像 (pAET) 技术与应用

发展基于叠层衍射与三维断层成像相结合的显微技术新方法，推动铁电拓扑晶体学向高精度、全元素、三维度发展。

4、新型铁电拓扑结构的外场响应与器件构建

探索极性拓扑结构在外场作用下的响应行为，探索极性拓扑结构在存储、通信、传感以及集成光子学中的应用。

新入职员工简介

刘娇龙，女，助理工程师，2022 年毕业于兰州理工大学材料科学与工程学院，获学士学位。同年，进入西北工业大学材料学院，2025 年获得硕士学位。于2025年6月入职松山湖材料实验室大湾区电镜中心。硕士期间主要进行变形铝镁合金微观组织与力学性能方面的研究。以第一作者身份在 Journal of Materials Science、Materials 和铸造技术期刊上发表 3 篇学术论文。获西北工业大学硕士优秀毕业生、甘肃省三好学生、兰州理工大学校、院三好学生、国家励志奖学金、西北工业大学校一、二等奖学金、兰州理工大学校一、二等奖学金等荣誉。

高瑞祥，男，助理工程师，2025 年毕业于桂林电子科技大学材料与化工专业，获硕士学位；2022 年毕业于山东理工大学高分子材料与工程专业，获工学学士学位，同时辅修法学获双学位。硕士期间，担任桂林电子科技大学 SEM/XRD 协管员，具备相关设备操作与管理经验，期间获 3 项国家发明专利，研究方向为纳米材料与储能器件，制备 MXene 基复合材料用于柔性超级电容器。曾获山东省“互联网+”金奖、广西壮族自治区“挑战杯”铜奖等 10 余项竞赛奖励，以及山东理工大学学业一等奖学金、天之润奖学金、桂林电子科技大学学业一等奖学金等荣誉，获评山东理工大学优秀毕业生、桂林电子科技大学优秀学生。2025 年 6 月，入职松山湖材料实验室大湾区显微科学与技术研究中心，现任原位扫描电镜助理工程师。

孙璐瑶，女，助理工程师，1999 年 12 月出生于山东省日照市。2022 年毕业于山东理工大学化学化工学院，获得学士学位。2022 - 2025 年就读于福州大学化工学院，获得工学硕士学位。于 2025 年 8 月入职粤港澳量子科学研究中心，任聚焦离子束扫描电子显微镜助理工程师。孙璐瑶主要从事甘油氢解制 1,2-丙二醇催化剂及机理的研究，目前于 Recent Research Advances 发表一篇论文。硕士期间于中国福建化学工程科学与技术创新实验室担任科研助理，具备扎实的催化材料制备与表征基础，并获得福州大学一等奖学金等荣誉。

多阶铁电拓扑态研究取得重要进展 (Nature Communications 2025)

近日，大湾区显微科学与技术研究中心耿皖荣副研究员、朱银莲研究员、马秀良研究员等与浙江大学郭相伟博士、洪子健教授等合作在铁电拓扑晶体学研究方面进一步取得重要进展，他们在自组装、高密度 $BiFeO_3$纳米结构中观测到多阶极性径向涡旋，并成功通过尺寸调控和外部电场实现不同拓扑态的转换和拓扑电荷控制。这一发现为下一代高密度、多态非易失性存储器件的设计提供了新思路。相关成果于2025年3月21日发表在《自然·通讯》（Nature Communications）期刊。

拓扑态因其独特的物理性质和在信息存储、传输中的潜力，近年来成为凝聚态物理和材料科学的研究热点。在铁电材料中，具有可调拓扑电荷的纳米级拓扑结构被视为实现高密度、多态存储的关键。然而，此前研究多集中于低阶拓扑态，高阶结构的稳定与调控仍面临挑战。

研究团队通过前期薄膜体系设计、后期精密调控边界条件及生长工艺，在 $BiFeO_3$薄膜中成功诱导出多阶极性径向涡旋。基于高密度、自组装纳米结构的薄膜构型，研究人员直接观测到具有独特极化分布组态的二阶径向涡旋，其表现为具有“甜甜圈”状面外分量和四象限式面内分量的极化组态，实现净拓扑电荷 $Q = 0$。通过改变 $BiFeO_3$纳米结构尺寸，进一步稳定了从一阶到三阶的多阶铁电径向涡旋，并实现了拓扑电荷的多态调控。利用压电力显微镜针尖施加的局部电场，实现了不同拓扑态的动态切换和拓扑电荷的连续变化。该研究结果为下一步构筑复杂极性拓扑组态，丰富铁电拓扑构型，进而设计新型多态铁电存储提供了新的可能性。

该研究得到了国家自然科学基金、广东省基础与应用基础研究基金、中国博士后科学基金、广东省量子科学战略计划、松山湖科学城显微科学与技术开放课题等多个项目的共同资助和支持。（原文附后）

利用界面对称性实现极化拓扑畴的精准调控(Advanced Functional Materials 2025)

近日，大湾区显微科学与技术研究中心冯燕朋副研究员、朱银莲研究员、马秀良研究员等在铁电极化拓扑畴调控方面取得了重要进展，他们通过巧妙地设计异质薄膜界面的对称性，成功实现了铁电极化布洛赫点(Bloch point)和半子(meron)结构的精准调控。相关成果于2025年6月23日在线发表于《Advanced Functional Materials》期刊上。

铁电极化拓扑畴具有纳米级三维尺寸，展现出拓扑保护、负电容、电导等特殊功能特性，在高密度、非易失性、低功耗信息存储器领域具有广泛的应用前景。然而，铁电拓扑畴的精准调控，尤其是在电子器件架构中如何稳定铁电极化拓扑畴仍面临挑战，因为在电子器件中不可避免受到异质界面的影响。

该研究团队在前期工作(Nature Materials, 2020；Nature Communications, 2024)的基础上，通过生长具有对称性界面以及非对称性界面的 $PbTiO_3$ 多层膜及超晶格，利用像差校正透射电子显微镜观察到对称性界面能有效稳定极化布

洛赫点，而非对称界面则更有利于极化半子拓扑畴的形成。相场模拟进一步揭示，这两种拓扑畴的稳定主要受到弹性能和静电能的影响，并且论证了不同薄膜之间的功函数差异在 $PbTiO_3$ 层内产生不同的内建电场，导致铁电极化发生择优排列，从而影响拓扑畴的形成与稳定。此外，压电力显微镜测试表明，极化布洛赫点的稳定能显著提高铁电薄膜的压电性能。本项工作揭示了界面对称性与拓扑畴极化对称性之间的强耦合关系，提出了一种基于异质界面调控铁电极化拓扑畴的新思路，为新型拓扑畴的调控以及不同拓扑畴之间的三维集成提供了新的方法。

该研究得到了国家自然科学基金、广东省基础与应用基础研究基金、广东省量子专项基金等项目的资助。（原文附后）

构筑纯奈尔型铁电斯格明子(Advanced Materials 2025)

近日，松山湖材料实验室大湾区显微科学与技术研究中心马秀良团队在铁电材料拓扑结构研究领域进一步取得重要进展，通过巧妙地调控静电能和梯度能的耦合关系，在 2 个单胞厚的 $PbTiO_3$ 薄膜中观测到了纯奈尔型斯格明子结构，这一发现为下一代高密度非易失性存储器件的超薄化设计提供了全新思路。相关成果发表于 Advanced Materials 期刊上。

在过去的五年中，从实验和理论两个方面对铁电斯格明子-泡泡（ferroelectric skyrmion-bubbles）进行了系统性探索，揭示了斯格明子-泡泡的形成是由块体能、梯度能、弹性能和静电能之间复杂相互作用共同决定的。这些斯格明子-泡泡展现出了诸如手性、负电容效应以及拓扑相变行为等。然而，与 Dzyaloshinskii-Moriya 相互作用不同，偶极子-偶极子相互作用是无手性的，这意味着它们在能量上更倾向于形成布洛赫型斯格明子。铁电奈尔型斯格明子的形成需要显著的电荷积累，以补偿电极化径向梯度的散度。因此，奈尔型斯格明子存在的可能性较低，这也使得探测与研究它们更具有挑战性。

在此，我们通过研究 $[(PbTiO_3)_n/(SrTiO_3)_n]_1$ 双层膜中斯格明子-泡泡随厚度的演化，观察到在厚度为 2 个单胞的超薄双层膜中纯奈尔型斯格明子的原子形态，其拓扑荷为 1。通过极化分析、几何相位分析和 X 射线 3D 倒易空间映射(RSM)相结合的实验手段，确认了这种纯奈尔型斯格明子的存在。研究发现，当双层膜的厚度从 50 个单胞降低到 2 个单胞时，同时具备奈尔和布洛赫特征的斯格明子-泡泡结构中的布洛赫特征完全消失，仅保留纯奈尔型斯格明子特征。通过相场模拟揭示了奈尔型斯格明子的形成机制，计算表明静电能和梯度能变化在稳定奈尔型斯格明子相中起到了关键作用。这些纳米尺度的纯奈尔型斯格明子代表了磁性对等物的电学等价物，拓展了拓扑相的尺寸极限，并为铁电物理学领域的进一步发展提供了潜在的推动力。

该研究得到了国家自然科学基金、博新计划、博后面上等多个项目的共同资助和支持。（原文附后）

nature communications

Article

https://doi.org/10.1038/s41467-025-58008-w

Observation of multi-order polar radial vortices and their topological transition

Received: 13 June 2024

Accepted: 10 March 2025

Wan-Rong Geng[1,8], Xiangwei Guo[2,8], Yin-Lian Zhu[1,3], Desheng Ma[4], Yun-Long Tang[5], Yu-Jia Wang[5], Yongjun Wu[2], Zijian Hong[2] & Xiu-Liang Ma[1,6,7]

Topological states have garnered enormous interest in both magnetic and ferroelectric materials for promising candidates of next-generation information carriers. Especially, multi-order topological structures with modulative topological charges are promising for multi-state storage. Here, by engineering boundary conditions, we directly observe the self-assembly two-order ferroelectric radial vortices in high-density $BiFeO_3$ nanostructures. The as-observed two-order radial vortex features a doughnut-like out-of-plane polarization distribution and four-quadrant in-plane distribution, with the topological charge of $Q = 0$. Systematic dimensional control of the $BiFeO_3$ nanostructures reveals size-dependent stabilization of distinct topological states, from elementary one-order to complex three-order radial vortices, which is further rationalized by phase-field simulations. The transition between different topological states with various topological charges is also realized under an external electric field. This study opens up an avenue for generating configurable polar topological states, offering potential advancements in designing high-performance multi-state memory devices.

The configurable spin topological defects in magnetic materials have been proven to be the source of many exotic phenomena with potential applications in electronic devices[1–3]. Complex topological structures are generally characterized by their topological charge Q, defined as a measure of the wrapping of spin vectors around a unit sphere, which governs the stability and dynamics of the topological states[4–6]. While numerous topological textures have been extensively studied, the majority exhibit topological charges confined to $|Q| \leq 1$. For example, (anti)skyrmion, known as the nanoscale spin vortex characterized by non-trivial real-space topological configuration[2,5], stands as the prototypical topological state with $Q = \pm 1$. It has been reported that this topological entity can undergo fractionalization into (anti)meron pairs bearing the fractional topological charge of $Q = \pm \frac{1}{2}$ (ref. 7). Besides, the (anti)vortex is another kind of ubiquitous topological defects with $Q = \pm 1$ (ref. 7). These spin structures display a variety of exotic characteristics, including robust topological protection[7] and self-organized lattice ordering[8,9].

Based on these topological sates, the modulation of topological charges enables the promising applications in high-density memory and neuromorphic computing[10,11]. Especially, the stabilization of the skyrmion bundles, the multi-Q three-dimensional skyrmionic textures, realizes the precise tuning of collective topological charges reaching $Q = 55$ (ref. 12). Similarly, the family of target skyrmion consisting of a central skyrmion surrounded by one or more concentric helical stripes[13] could also realize the alternative topological charges. As one intriguing member of the target skyrmion family[13], skyrmionium, with

---

[1]Bay Area Center for Electron Microscopy, Songshan Lake Materials Laboratory, Dongguan 523808, China. [2]State Key Laboratory of Silicon and Advanced Semiconductor Materials, School of Materials Science and Engineering, Zhejiang University, Hangzhou 310058, China. [3]Hunan University of Science and Technology, Xiangtan 411201, China. [4]School of Applied and Engineering Physics, Cornell University, Ithaca, NY 14850, USA. [5]Shenyang National Laboratory for Materials Science, Institute of Metal Research, Chinese Academy of Sciences, Shenyang 110016, China. [6]Institute of Physics, Chinese Academy of Sciences, Beijing 100190, China. [7]Quantum Science Center of Guangdong-HongKong-Macau Greater Bay Area (Guangdong), Shenzhen 510290, China. [8]These authors contributed equally: Wan-Rong Geng, Xiangwei Guo. e-mail: hongzijian100@zju.edu.cn; xlma@iphy.ac.cn

the doughnut-like out-of-plane (OOP) spin texture[14–17], exhibits a vanishing net topological charge ($Q = 0$), largely suppressing the detrimental effect of skyrmion Hall effect[14].

While magnetic topological states and the control of topological charges have been extensively studied, the emergent topological domains in ferroelectrics have recently garnered significant attention as their promising applications for high-density data storage[18], as well as ultralow power negative capacitance field effect transistors[19]. By elaborately regulating the interplay of elastic, electrostatic and gradient energies in the dedicated ferroelectric systems, several complex topological states and topological orderings could be stabilized[20–30]. For example, the vortices, orderly stabilized in $PbTiO_3/SrTiO_3$ superlattices[21], display interesting functionalities distinct from the bulk domains, such as negative capacitance[31], emergent chirality[32] and special subterahertz collective mode-vortexon[33]. Furthermore, the thermal responses of polar vortices exhibit a wealth of intermediate states thereby triggering multi-state switching of ferroelectric topologies[34]. Despite the remarkable progress in ferroelectrics, the existing studies predominately focus on the low-order polar topological structures, leaving the high-order configurations with tunable topological charges largely unexplored.

Herein, the stabilization and modulation of ferroelectric two-order radial vortex and the topological transition between multi-order vortices are observed in high-density self-assembly $BiFeO_3$ (BFO) nanostructures. Piezoresponse force microscopic (PFM) and aberration-corrected scanning transmission electron microscopic observations indicate that the polarization configuration of ferroelectric two-order radial vortex with the topological charge of $Q = 0$ features a doughnut-like OOP texture and four-quadrant in-plane (IP) distribution. Furthermore, multi-order radial vortices with different topological charges, including one-order radial vortex and three-order radial vortex, can also be stabilized by tuning the sizes of BFO nanostructures, confirmed by phase-field simulations. The transition between different topological states could be realized via the assistance of external electric field imposed by PFM scanning probes. This work not only enriches the family of observed topological structures in ferroelectrics, but also provides a unique and effective way of designing intriguing topological structures through boundary condition engineering.

Results

As one of the most extensively studied multiferroic materials, BFO is known to exhibit rich functionalities and various domain structures[35–37]. In particular, the topological states including the center-type domains[29,38], vortices[22,39] and bimerons[40] have been reported in confined BFO systems. To explore the promising possibility of polar topological states, 14.5 nm thick BFO films were grown on [001]-oriented $(LaAlO_3)_{0.29}(SrTa_{1/2}Al_{1/2}O_3)_{0.71}$ (LSAT) substrates, displaying the as-grown high-density self-assembly nanoislands (Fig. 1a). The averaged lateral size of the nanoislands is about 350 nm (Fig. 1a). The epitaxial nature of the BFO film is verified by the X-ray diffraction (XRD) scan (Fig. 1b) and the reciprocal space map (RSM) result (Fig. 1c). As revealed in Fig. 1c, the coexistence of rhombohedral BFO (R-BFO) and tetragonal-like BFO (T-like BFO) is stabilized in the film under the large compressive strain of 2.4% imposed by LSAT substrate. The domain structures of the BFO nanoislands are characterized by vector mode of PFM, which allows the simultaneous mapping of the vertical and lateral signals, including the amplitude and phase. As shown in Fig. 1d–f, the vertical PFM amplitude (V-amp.) and phase (V-pha.) images display as the doughnut-like OOP contrast for one nanoisland. The nanoisland constitutes of two parts: the yellow-colored core and the brown-colored periphery. Around the nanoislands, the flat BFO film share the same OOP phase contrast with the cores of nanoislands, which is further confirmed by the height and vertical PFM phase spacing profiles in Fig. 1h, i for one nanoisland (Fig. 1g). The result in Fig. 1i suggests the alternative OOP polarization distribution in the manner of downward-upward-downward from flat BFO film, nanoisland periphery to nanoisland core.

To further resolve the 3D polarization distribution, a series of vector PFM mapping was conducted according to the method proposed previously[38,41] to determine the IP polarization distribution in the BFO nanostructures. The detailed reconstruction procedure is demonstrated in Fig. 2, with more details shown in Supplementary Fig. 1. The OOP polarization distribution for one nanoisland is revealed in Fig. 2a, showing the doughnut-like contrast. Then, by rotating the sample clockwise for 0°, 45° and 90° relating to the cantilever of PFM tips, the lateral PFM phases of the nanoislands at different angles can be found in Fig. 2b–d, displaying as the half-dark and half-bright contrast. Thus, the IP polarization distribution of one nanoisland is constructed as the unique domain structure of center-divergent or center-convergent arrangement. The special polarization distribution is prevalent in the high-density nanoisland array in the BFO film, with the detailed PFM analyses being displayed in Supplementary Fig. 1. Furthermore, the polarization distribution of one nanoisland is also confirmed by the high-angle annular dark-field imaging under the scanning transmission electron microscopy mode (HAADF-STEM) using Cs-STEM. For the IP direction, the polarization of one nanoisland displays as the four-quadrant contrast, which is further determined to be the center-divergent state, as shown in the low-magnification HAADF-STEM images (Fig. 2e, f) and atomic-resolved HAADF-STEM images (Fig. 2g–j). For the OOP direction, the polarization is in the direction of downward at the core of nanoisland (Supplementary Fig. 2-3). Thus, the polarization of one nanoisland is in the distribution of downward-upward from the core to the periphery of the nanoisland (Supplementary Fig. 4), with the polarization being continuous rotation. The OOP polarization for the surrounding matrix region (SMR) around the nanoisland is further determined as the downward direction (Supplementary Fig. 5). By combining the doughnut-like OOP polarization distribution (top panel in Fig. 2k) and four-quadrant IP polarization distribution (bottom panel in Fig. 2k and Supplementary Fig. 6), the three-dimensional polarization distribution for the combined area (CA) consisting of one nanoisland and SMR could be reconstructed, as schematized in Fig. 2l–n, which is reminiscent of the skyrmionium to some extent[13]. However, considering the fact that the polarization changes from core region to SMR region in the BFO nanostructures are not strictly calculated as 2π, the polarization state is thereby defined as the ferroelectric two-order radial vortex, displaying as two nested concentric vortices. Meanwhile, the ferroelectric two-order radial vortex is expected to enrich the polar topological states and exotic physical phenomena in ferroelectric materials. The spontaneous occurrence of the polar two-order radial vortex in the as-grown BFO nanostructures implies that it is the favorable state stabilized by boundary condition engineering, which is observed prevalently in BFO film. The formation of this topological state could be attributed to the combined contributions of depolarization field, strain relaxation and charge accumulation. On the one hand, the BFO films fabricated via high deposition flux tend to form the nanoislands[38,41]. At the core of the nanoislands, the elemental non-stoichiometry of Bi and Fe in Supplementary Fig. 7 is expected to from the atomic inter-diffusion between the film and the substrate during the film deposition and the annealing procedure due to the spontaneously formed dipole disclinations in the cores of the nanoislands[41–44]. Thus, the charge is accumulated due to the elemental difference (Supplementary Fig. 7), oxygen vacancies or other potential charged carriers[45,46], thereby stabilizing the tail-to-tail charged domain walls and forming the center-divergent polarization along in-plane direction (Fig. 2e–j). On the other hand, the coupling effects between the depolarization field and the lattice mismatch strain at heterointerface in the BFO films stabilize the alternative out-of-plane polarization distribution, with the nanoisland cores as the preferred nucleation sites of ferroelastic domains. As a

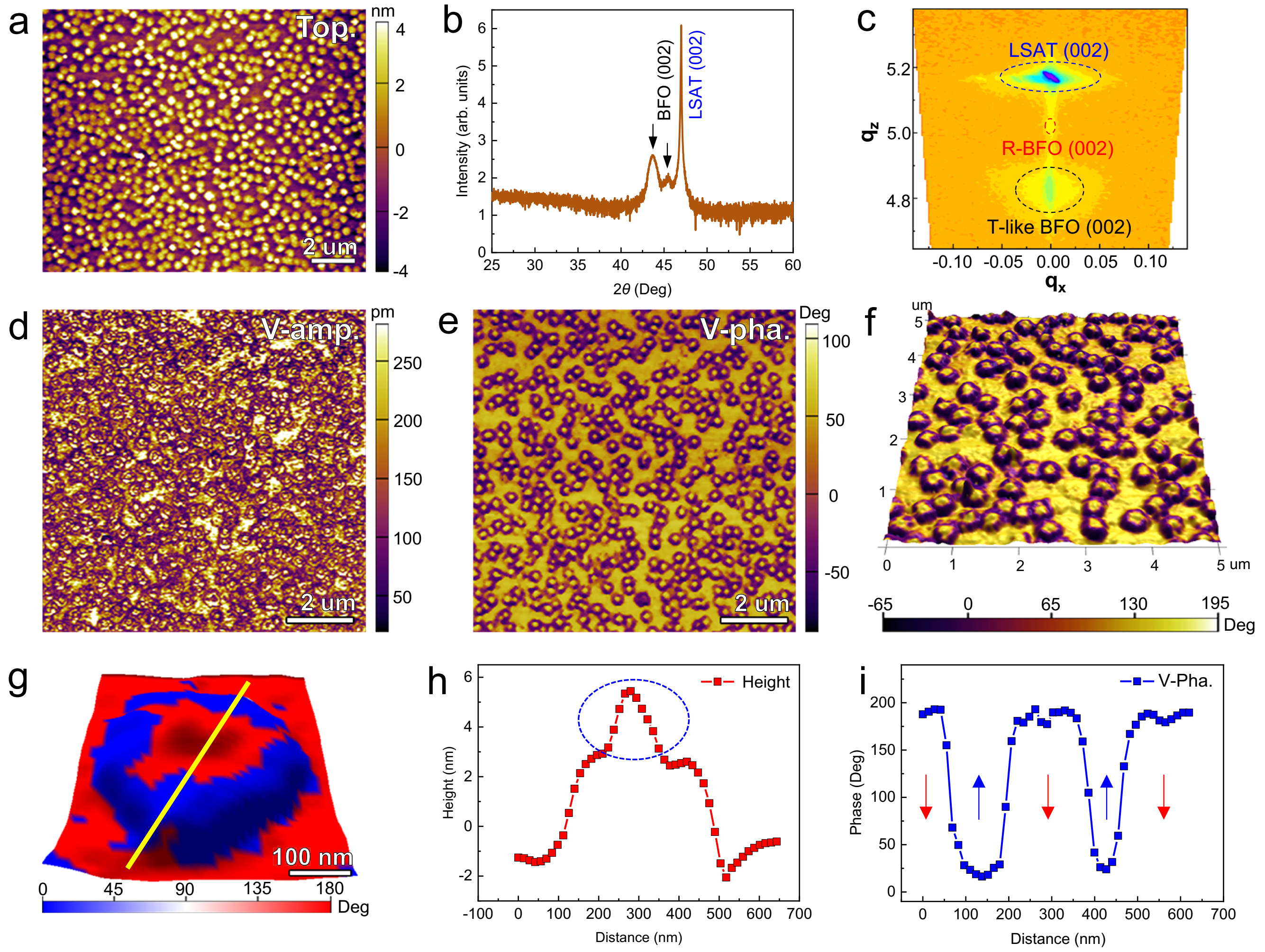

Fig. 1 | PFM analyses of high-density BFO nanoislands. **a** Topography of BFO (001) thin film with self-assembled nanoislands. **b** X-ray diffraction results showing the pseudocubic 002 peaks of the films. **c** Reciprocal space map recorded around the LSAT 002 Bragg peaks. **d, e** Vertical PFM amplitude (V-amp.) and vertical PFM phase (V-pha.) images of the domain patterns in the BFO film. **f** Enlarged OOP phase image superimposed with the topography image. **g** OOP phase image of one BFO nanoisland. **h, i** Height and vertical PFM phase spacing profiles along the yellow line in (**g**). The hump denoted by blue ellipse in (**h**) is derived from the additional adsorbates from air.

result, the two-order radial vortex with alternative out-of-plane polarization and center-divergent in-plane polarization is obtained in the BFO films.

Furthermore, the polarization configurations of the nanostructures can be modulated by the size of the nanostructures (defined in Supplementary Fig. 8), thereby generating multiple polar topological states, as summarized in Supplementary Table 1. In Fig. 3 and Supplementary Fig. 9-11, three kinds of polarization patterns are revealed, with the averaged sizes of nanoislands changing from 100 nm, 200 nm to 400 nm. For the case of 100 nm nanoislands, the morphology, vertical amplitude and phase images are displayed in Supplementary Fig. 9 and Fig. 3a, b. The uniform phase contrast is observed inside the nanoislands, which is surrounded by the different phase contrast of the SMR. Figure 3c is the phase spacing profile for one nanostructure (inset in Fig. 3b), suggesting the nearly 180° out-of-plane phase difference between two regions. The arrows in Fig. 3c suggest the opposite OOP polarization directions. The IP polarization distribution for the nanoisland displays the similar center-divergent pattern as the case of 350 nm nanoisland. By combining the IP and OOP polarization distribution, the 3D polarization pattern of the CA is constructed as one-order radial vortex (Fig. 3d), with the change of azimuth angle being 0.5π (Supplementary Fig. 12a). The CA includes the single nanoisland (inside the solid circle) and SMR (region between solid circle and dotted circle) shown in the inset in Fig. 3d. Increasing the size of nanoisland to 200 nm (see the morphology image in Supplementary Fig. 10), the vertical amplitude and phase images of the nanoislands and the SMRs display the different contrast, as shown in Fig. 3e, f. The similar doughnut-like OOP polarization distribution is revealed inside the nanoislands (Fig. 3f), but with the SMR sharing the same vertical phase contrast as the nanoisland periphery, which is further confirmed by the phase spacing profile in Fig. 3g. As a result, the polarization pattern for the CA including the 200 nm nanoisland is also reconstructed and defined as the one-order radial vortex, also with the change of azimuth angle being 0.5π (Supplementary Fig. 12b). When the averaged size of the nanoisland is 400 nm (see the morphology image in Supplementary Fig. 11), the vertical phase contrast nearly displays as the doughnut-like OOP polarization distribution reminiscent of the two-order radial vortex in Fig. 1e, excluding the emergence of the localized opposite OOP phase in the middle of nanoisland core (Fig. 3i, j). As shown in Fig. 3k, l, the phase change of the OOP polarization from the center of the nanoisland core to the SMR is calculated as 2.5π (Supplementary Fig. 12d). Thereby, the constructed polarization pattern in Fig. 3l is defined as the three-order radial vortex. In a word, by changing the size of nanostructures, three kinds of polar topological states are stabilized, including the one-order radial vortex, two-order radial vortex and three-order radial vortex. It is

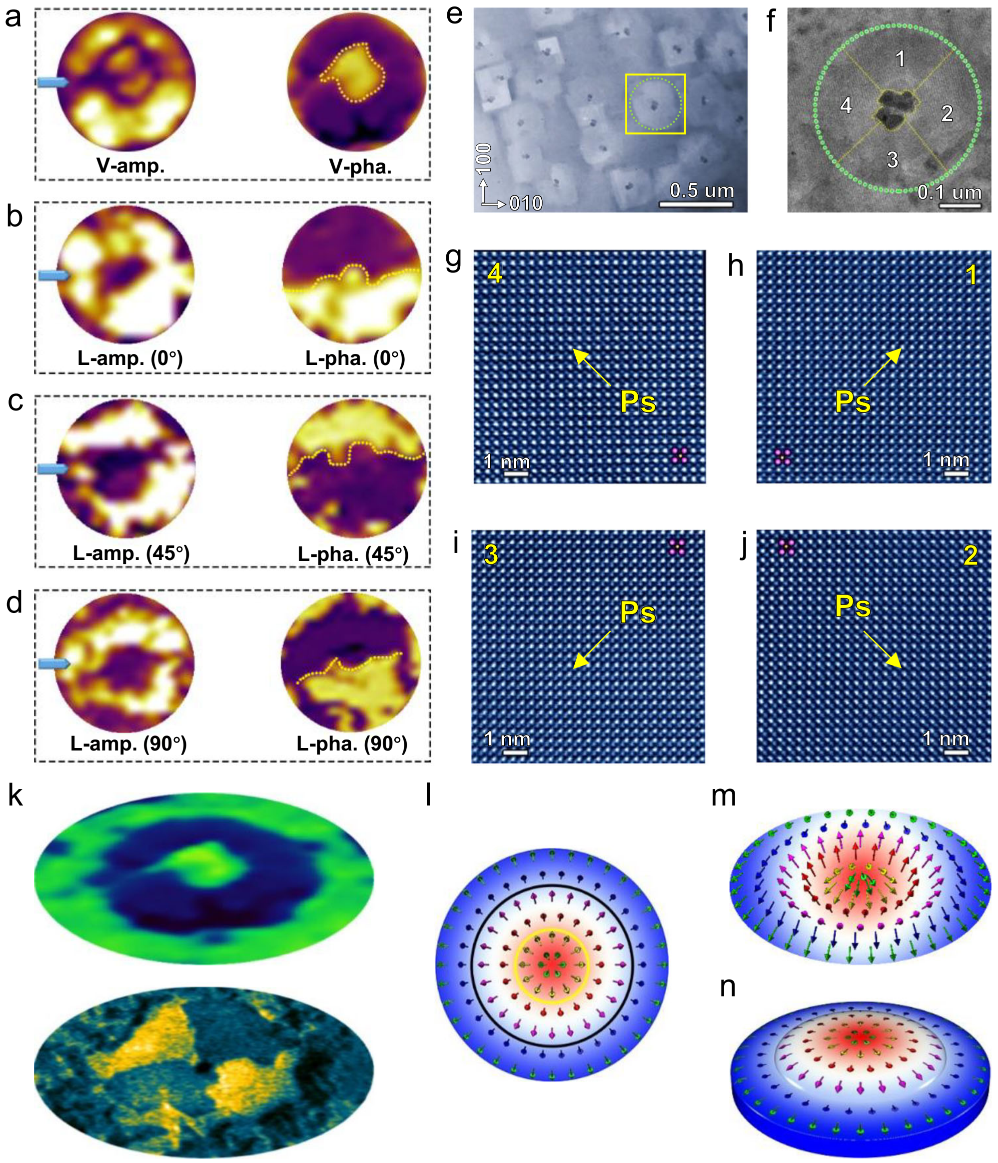

Fig. 2 | Reconstructed polar two-order radial vortex in one nanostructure. **a** The vertical PFM amplitude (V-amp.) and vertical PFM phase (V-pha.) images of one nanoisland. **b**–**d** The lateral PFM amplitude (L-amp.) and lateral PFM phase (L-pha.) images of one nanoisland with sample rotation for 0° (**b**), 45° (**c**) and 90° (**d**), respectively. Blue arrows in (**a**–**d**) denoting the cantilevers of PFM tips. **e** A planar-view HAADF-STEM image showing the nanoislands in BFO film. **f** Enlarged HAADF-STEM image for one nanoisland. **g**–**j** Polarization distribution of BFO corresponding to the regions numbered 1, 2, 3 and 4 in (**f**), respectively. **k** Enlarged V-pha. image (top panel) and HAADF-STEM image (bottom panel) around one nanoisland, displaying the out-of-plane and in-plane polarization distribution, respectively. **l**–**n** Reconstructed 3D polarization distribution around one nanoisland, suggesting the polar topological state of two-order radial vortex.

worthwhile noting that the nanoislands would merge with each other and form the flat surface in thicker BFO films (about 20 nm), thereby stabilizing the labyrinthine domains, as shown in Supplementary Fig. 13.

The evolution of domain pattern and their topological features with diameter of the BFO nanoislands are further investigated by the phase-field simulations (details in Methods). The schematic of the phase-field model for the disc-shaped BFO nanostructures is shown in Supplementary Fig. 14. To mimic the experimental conditions, three different sizes of the disc-shaped BFO nanostructures with diameters of d, $2\,d$, and $3\,d$ are simulated and compared, as shown in Fig. 4a–c. It should be admitted that the theoretical transition size is slightly smaller than the experimental size, which can be attributed to a higher theoretical depolarization field where the perfect charge screening is assumed. However, it can be clearly seen that the trend for the size dependent transition agrees remarkably well. With a priori setting of the 180° circular domains and a subsequent annealing treatment analogous to the experimental preparation, different topological structures were formed in the three BFO nanostructures (Fig. 4d–f). Single doughnut-like circular domains can be stabilized in the BFO nanostructure when the diameter is d, similar to the bubble-like structure observed in the PTO/STO system[24]. The planar distribution of OOP polarization and surface integration of the Pontryagin density reveals that this circular domain structure is a polar one-order radial vortex (Fig. 4d). As the nanostructure diameter increases from d to $2\,d$, the double nested doughnut-like domain could also be formed in the BFO nanostructure, confirming the formation of polar two-order radial vortex (Fig. 4e). Notably, when the nanostructure diameter further increased to $3\,d$, a triple nested circular domain pattern occurs in the BFO nanostructure (Fig. 4f). In this case, such structure is determined to be a three-order radial vortex. The local OOP polarization distribution of the BFO nanostructures with the three sizes are plotted (Fig. 4g–i), showing the stabilization of three different topological phase features, i.e., one-order radial vortex, two-order radial vortex,

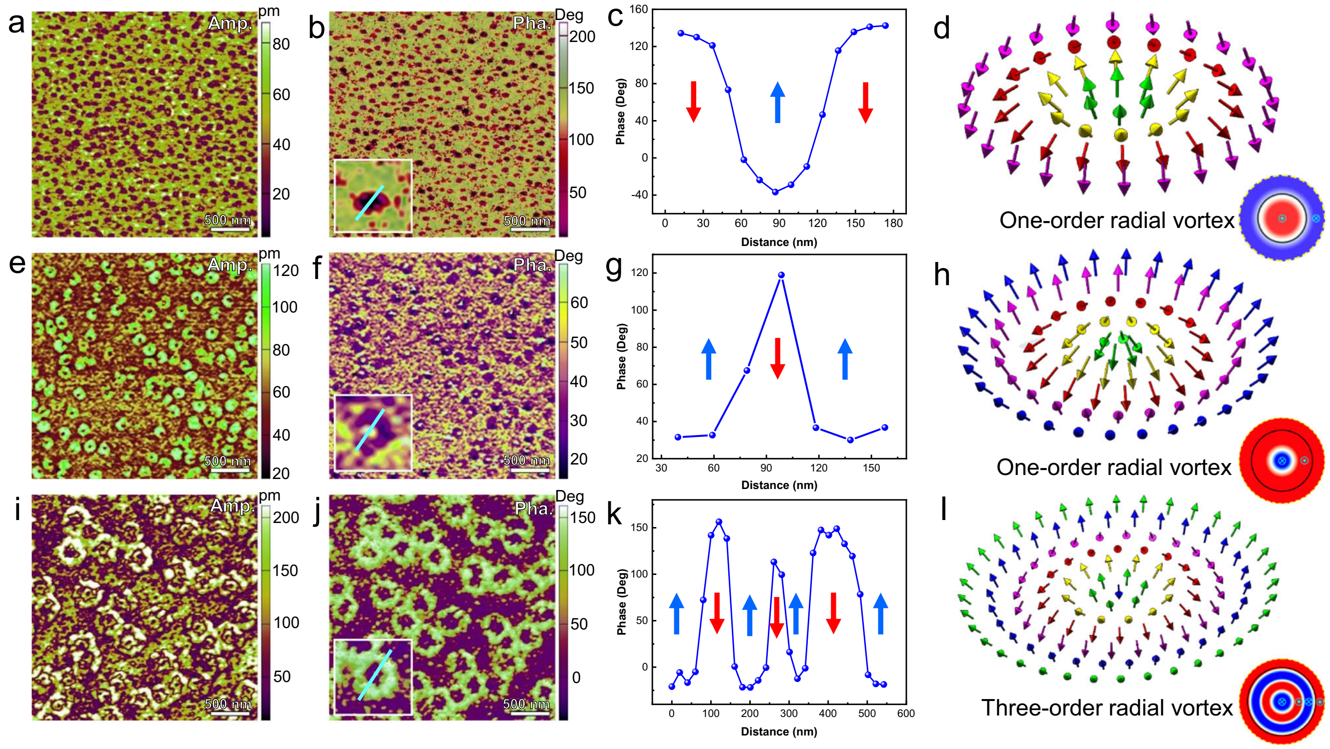

Fig. 3 | Topological transition as a function of the sizes of nanoislands. a–b V-amp. and V-pha. images of the BFO film with the averaged size of nanoislands being 100 nm. **c** Phase spacing profile around one nanoisland in the inset of (**b**). **d** Reconstructed 3D polarization pattern of one-order radial vortex. The schematic at the bottom right corner showing the OOP polarization distribution around one nanoisland. **e, f** V-amp. and V-pha. images of the BFO film with the averaged size of nanoislands being 200 nm. **g** Phase spacing profile around one nanoisland in the inset of (**f**). **h** Reconstructed 3D polarization pattern of one-order radial vortex. The schematic at the bottom right corner showing the OOP polarization distribution around one nanoisland. **i, j** V-amp. and V-pha. images of the BFO film with the averaged size of nanoislands being 400 nm. **k** Phase spacing profile around one nanoisland in the inset of (**j**). **l** Reconstructed 3D polarization pattern of three-order radial vortex. The schematic at the bottom right corner showing the OOP polarization distribution around one nanoisland.

and three-order radial vortex by varying the size of the nanostructures, which agrees qualitatively well with the experimental observations.

To further gain physical insights into the creation mechanism for these multi-order radial vortices, different energy contributions within the one-order, two-order and three-order radial vortices in BFO nanostructures were investigated from phase-field simulation. For simplicity, the BFO nanodisk diameter was fixed at 3 *d* to analyze the individual energy density differences among pre-designed one-order, two-order and three-order radial vortices. As shown in Supplementary Fig. 15, increasing the vortex order from one-order to three-order introduces more domain walls, raising the gradient energy. However, this is effectively compensated by reductions in Landau, electrostatic, and elastic energies, which relieve system strain and efficiently screen the depolarization field, allowing the three-order radial vortex to stabilize. Therefore, from a theoretical perspective, the Landau energy, elastic energy, and electrostatic energy could serve as the driving forces for multi-order radial vortex formation in BFO nanostructures.

To illuminate the polarization switching behaviors of the polar two-order radial vortex in Fig. 2, localized PFM phase-field hysteresis loops and amplitude-field butterfly loops are compared in Supplementary Fig. 16 for three representative regions, including the nanoisland core (numbered region 1), nanoisland periphery (numbered region 2) and SMR (numbered region 3). The localized coercive fields for three regions could be obtained from PFM phase-field loops and PFM amplitude-field loops in Supplementary Fig. 16b-d. The coercive field of nanoisland core in Supplementary Fig. 16b is calculated as 4500 kV/cm, which is larger than that of nanoisland periphery (2264 kV/cm in Supplementary Fig. 16c) and SMR (3500 kV/cm in Supplementary Fig. 16d), suggesting the tougher possibility of polarization switching at the same applied field. Then the topological transitions in BFO films are further discussed under the stimulation of external electric fields. The vertical PFM phase images of the initial state and poled state by the *dc* bias voltages of +40 V and -40V are displayed in Fig. 5a–c, indicating that the changed OOP polarization distribution for the nanostructures including the nanoislands and the SMR. To elucidate the detailed topological transitions modulated by *dc* bias electric field, three kinds of topological transitions are highlighted by red (Type 1), green (Type 2) and yellow (Type 3) circles in Fig. 5a–c. The changes of OOP polarization distribution and topological transitions are further schematized in Fig. 5d–i. For the Type 1 in Fig. 5d, e and Supplementary Fig. 17a, the initial domain state of one nanostructure is three-order radial vortex. After the electrical writing experiment using the voltage bias of 40 V, the three-order radial vortex transforms into the non-topological domain (abbreviated as NTD). Then after additional stimulation of -40 V at the same region, the domain state of the nanostructure is stabilized as two-order radial vortex. During this process, the topological charge changes from $|Q| = 0.707$ to $|Q| = 0$ and finally $|Q| = 0$ (Supplementary Fig. 18a). For the Type 2 in Fig. 5f, g and Supplementary Fig. 17b, the topological transition process modulated by opposite voltage bias is determined to be from two-order radial vortex to NTD and finally switching back to two-order radial vortex, accompanying with topological charge remaining constant ($|Q| = 0$) (Supplementary Fig. 18b). For the Type 3 in Fig. 5h, i and Supplementary Fig. 17c, the transition from two-order radial vortex to NTD and finally one-order radial vortex is schematized, with the topological charge changing from $|Q| = 0$ to $|Q| = 0$ and finally $|Q| = 0.707$, as shown in Supplementary Fig. 18c. As a result, three kinds of topological transitions could be concluded under the stimulation of opposite voltage bias. The concomitant changes of topological charges (Supplementary Fig. 18) suggest the feasibility of employing the

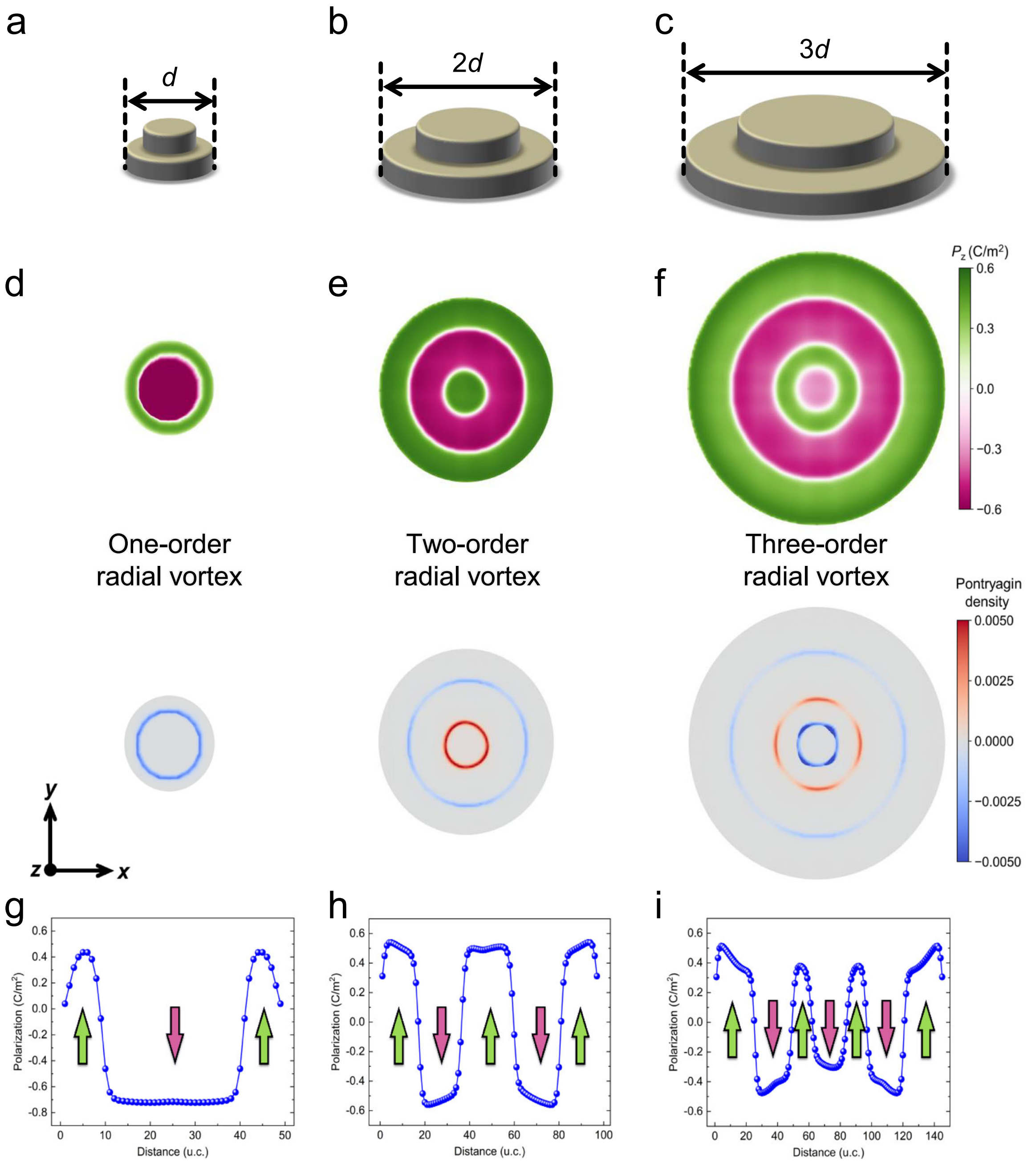

Fig. 4 | Phase-field simulations of polar topological structures of BFO islands with different diameters. a–c Schematics of the nanostructures including the disc-shaped BFO islands and the surrounding BFO matrix, with the diameters of the nanostructures being *d*, 2 *d*, and 3 *d*, respectively. **d–f** Planar view of out-of-plane polarization and Pontryagin density distributions in BFO nanostructures with diameters of *d*, 2 *d*, and 3 *d*. **g–i** The local out-of-plane polarization distributions along a horizontal line through the center of BFO nanostructures with diameters of *d*, 2 *d*, and 3 *d*.

topological charges as the digital bits in the promising vortex-based multistate nonvolatile memory devices[10].

In summary, we report the observation of self-assembled polar two-order radial vortex and other multi-order radial vortices in high-density $BiFeO_3$ nanostructures through boundary condition engineering. The polar two-order radial vortex, exhibits a doughnut-like pattern of out-of-plane polarization and four-quadrant in-plane polarization. Furthermore, by combining the phase-field simulations, it is confirmed that the topological states could be tuned by varying the size of the BFO nanostructures. Multi-order radial vortices with adjustable topological charges, such as the one-order radial vortex and three-order radial vortex, have been stabilized in nanostructures of different sizes. Transitions between these topological states can also be achieved under the application of an external electric field. The discovery of polar two-order radial vortex and the transition between various multi-order radial vortices highlight the rich diversity of topological structures and offer a promising strategy for multi-state, non-volatile ferroelectric memory devices.

Methods

Film deposition details

Using pulsed laser deposition (PLD) with a Coherent ComPex PRO 201 F KrF ($\lambda = 248$ nm) excimer laser, a series of epitaxial BFO thin films on LSAT (001) substrates were deposited. The LSAT (001) substrates used here are commercial substrates without extra chemical or heat treatment. Before deposition, the substrates were dipped in the 90% alcoholic solution for 12 hours to clean the organic pollutant and dusts. The substrates were affixed in the substrate plate using the silver paint

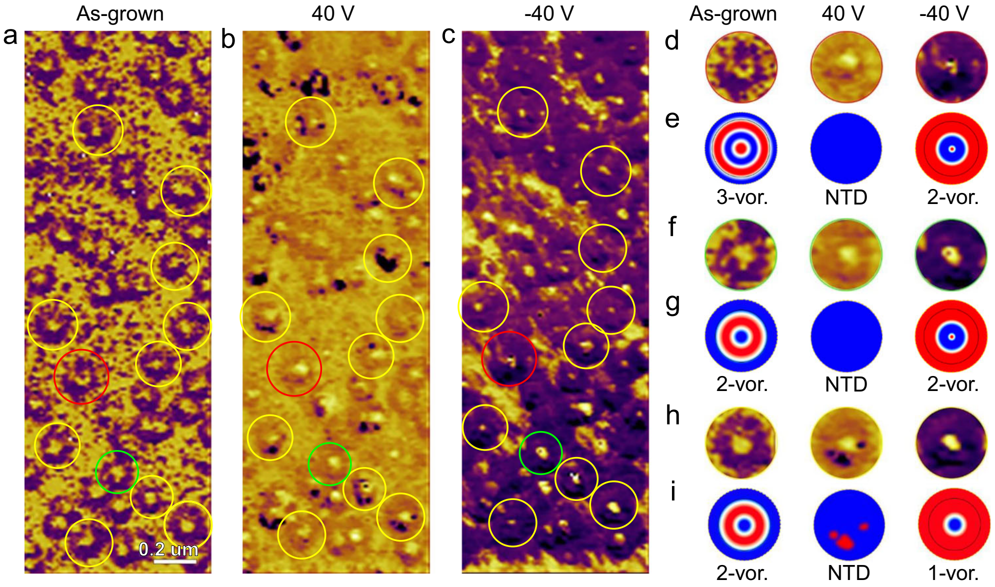

Fig. 5 | Changes of polarization patterns under external electric fields. a Vertical PFM phase image of the initial domain pattern. **b** Vertical PFM phase image after writing experiment with a voltage of 40 V. **c** Vertical PFM phase image after additional writing experiment with opposite voltage of −40 V. The red, green and yellow circles denote three kinds of topological transitions. **d** Enlarged vertical PFM phase images of one nanostructure highlighting by red circle in (**a**–**c**). **e** Corresponding schematics of (**d**), suggesting the transition from three-order radial vortex to NTD and finally radial vortex. **f** Enlarged vertical PFM phase images of one nanostructure highlighting by green circle in (**a**–**c**). **g** Corresponding schematics of (**f**), suggesting the transition from two-order radial vortex to NTD and finally two-order radial vortex. **h** Enlarged vertical PFM phase images of one nanostructure highlighting by yellow circle in (**a**–**c**). **i** Corresponding schematics of (**h**), suggesting the transition from two-order radial vortex to NTD and finally one-order radial vortex. The one-order, two-order and three-order radial vortices are abbreviated to 1-vor., 2-vor. and 3-vor., respectively.

solution and transferred into the main chamber of the PLD equipment. Then the substrates were heated to 850 °C for 20 minutes to clean the substrate surfaces and then cooled slowly down to the film deposition temperature at a rate of 5 °C min^{-1}. Before growing the BFO layers, the velocity for the substrate rotation motor and the target DC rotation motor were set to be 47 deg s^{-1} and 71 deg s^{-1}, respectively. At the same time, the raster motor mode was selected for the target carousel motor, with the maximum speed being 30 deg s^{-1} and minimum speed being 1 deg s^{-1}. The deposition of BFO films used the 1 mol% Bi-enriched BFO target, which was pre-sputtered for 20 minutes at 850 °C to clean the surface with the shutter being closed. When growing the BFO layers, the shutter was opened, a repetition rate of 8 Hz, substrate temperature of 800 °C, oxygen partial pressure of 12 Pa and laser energy of 2 J cm^{-2} were used. The distance between target and substrate was set to be 60 cm. Under the above deposition condition, the height of the laser plume was observed to be about the 1/2 of the distance between target and substrate. After deposition, these films were annealed at 800 °C in an oxygen partial pressure of 266 Pa for 20 minutes and then cooled slowly to room temperature at a rate of 5 °C min^{-1}.

PFM observations

The PFM characterization was performed using an Asylum Research Cypher S atomic force microscope (Oxford Instruments) at room temperature. Both vertical and lateral PFM images were simultaneously acquired through Vector PFM mode, with data validity cross-verified by Dual AC Resonance Tracking (DART) methodology. Ti/Ir (5/20)-coated conductive probes (ASYELEC-01-R, spring constant: 2.8 N/m) were employed, with contact resonance frequencies optimized at 350 kHz (vertical) and 760 kHz (lateral) through thermal noise calibration. Prior to local hysteresis measurements, cantilever sensitivity was rigorously calibrated via the GetReal method[47]. Domain switching dynamics were investigated by applying DC bias voltages in DART mode, while nanoscale domain lithography was executed through sequential voltage patterning using the AFM lithography mode.

TEM sample preparation

STEM specimens were prepared through a standardized mechanical processing process: bulk samples were sectioned, epoxy-bonded, mechanically thinned to <20 µm thickness, dimpled to <5 µm center thickness, and precision-finished via Ar$^+$ ion milling (Gatan 691 PIPS). To minimize beam-induced damages, a multi-stage ion milling strategy was implemented: initial coarse milling at 7° incidence angle and 4.5 keV with liquid nitrogen cooling, followed by a final low-energy polishing step (0.1 keV, 10 min, ±5° beam oscillation).

STEM observation

HAADF-STEM characterization was conducted using a double Cs-corrected ThermoFisher Spectra 300 (scanning) transmission electron microscope (CEOS probe/imaging correctors) operated at 300 kV. The probe semi-convergence angle was optimized to 25 mrad, with HAADF detector inner/outer collection angles set at 71/200 mrad to ensure optimal Z-contrast sensitivity.

STEM result analyses

The drift-corrected frame integration function was used for frame series in Velox software to create a single image, aiming to optimize contrast while minimizing beam-induced specimen drift artifacts. To enhance signal-to-noise ratio, raw HAADF-STEM images underwent Wiener deconvolution coupled with a low-pass frequency filter (cutoff at the instrument's theoretical resolution limit). Atomic column positions were quantitatively determined through sub-Å precision 2D Gaussian fitting implemented in MATLAB[48], enabling systematic mapping of B-site cation displacements.

X-ray diffraction and reciprocal space mapping

Crystallographic analysis was conducted using a high-resolution Bruker D8 Advance X-ray diffractometer (Cu Kα radiation source, λ = 1.5406 Å), employing θ-2θ scans and reciprocal space mapping to resolve the out-of-plane lattice parameters and phase structures.

Phase-field simulations

In the phase-field approach, the evolution of the order parameters spontaneous polarization vector (**P**) and oxygen octahedral tilt (**θ**) in the islands on the surface of BFO films grown on LSAT substrates is governed by the time-dependent Ginzburg-Landau equation:

$$\frac{\partial \phi}{\partial t} = -M\frac{\delta F}{\delta \phi} \tag{1}$$

where $\boldsymbol{\phi}$, t and M denote the order parameter (either **P** or **θ**), the evolution time step and the dynamic coefficient, respectively. The total free energy F of the BFO island has the contributions from the individual energy densities, i.e., the Landau/chemical, elastic, electrostatic, and polar/rotation gradient energy densities:

$$F = \int \left(f_{Landau} + f_{elastic} + f_{electric} + f_{gradient}\right) dV \tag{2}$$

Detailed expressions of these energy densities, materials parameters as well as the numerical simulation procedure are described previous reports[49–51].

The discrete grid points of $200\boldsymbol{\Delta x}\times200\boldsymbol{\Delta y}\times90\boldsymbol{\Delta z}$ with a grid spacing of 0.4 nm are used to describe the BFO system consisting of a disc-shaped nanoisland surrounded by matrix region, substrate and air layer (see Supplementary Fig. 14). Corresponding to the experimental results, three different sizes of BFO islands are considered and their diameters are set to the d, $2\,d$, and $3\,d$, with d being 48 grids, respectively. A thin STO dielectric layer is also introduced at the top and bottom of the BFO island to simulate the depolarization field effect at the interface. The total height of BFO island is 36 grids inside the simulation mesh. Periodic boundary conditions are assumed in the two in-plane dimensions of the entire model, while a superposition method is applied in the thickness dimension[52]. To simulate the evolution of polar radial vortices with disk diameter in BFO nanoislands, the initial set-up for the simulation is a series of the 180° circular domains with a small random noise ($<0.01\ \mu C/cm^2$). Then they relaxed to the stable states through an annealing process.

Reporting summary

Further information on research design is available in the Nature Portfolio Reporting Summary linked to this article.

Data availability

The data that support the findings of this study are provided in the article and the Supplementary Information. The data sets generated and analyzed during the current study are available from the corresponding author on reasonable request.

References

1. Fert, A., Cros, V. & Sampaio, J. Skyrmions on the track. *Nat. Nanotechnol.* **8**, 152–156 (2013).
2. Fert, A., Reyren, N. & Cros, V. Magnetic skyrmions: advances in physics and potential applications. *Nat. Rev. Mater.* **2**, 1–15 (2017).
3. Roessler, U. K., Bogdanov, A. & Pfleiderer, C. Spontaneous skyrmion ground states in magnetic metals. *Nature* **442**, 797–801 (2006).
4. Braun, H.-B. Topological effects in nanomagnetism: from superparamagnetism to chiral quantum solitons. *Adv. Phys.* **61**, 1–116 (2012).
5. Nagaosa, N. & Tokura, Y. Topological properties and dynamics of magnetic skyrmions. *Nat. Nanotechnol.* **8**, 899–911 (2013).
6. Nahas, Y. et al. Discovery of stable skyrmionic state in ferroelectric nanocomposites. *Nat. Commun.* **6**, 8542 (2015).
7. Junquera, J. et al. Topological phases in polar oxide nanostructures. *Rev. Mod. Phys.* **95**, 69 (2023).
8. Hagemeister, J., Romming, N., Von Bergmann, K., Vedmedenko, E. Y. & Wiesendanger, R. Stability of single skyrmionic bits. *Nat. Commun.* **6**, 8455 (2015).
9. Yu, X. Z. et al. Transformation between meron and skyrmion topological spin textures in a chiral magnet. *Nature* **564**, 95–98 (2018).
10. Du, G. et al. Design of polar skyrmion-based nanoelectronic prototype devices with phase-field simulations. *Adv. Funct. Mater.* 2405594 (2024).
11. Wang, Y. et al. Electric-field-driven non-volatile multi-state switching of individual skyrmions in a multiferroic heterostructure. *Nat. Commun.* **11**, 3577 (2020).
12. Tang, J. et al. Magnetic skyrmion bundles and their current-driven dynamics. *Nat. Nanotechnol.* **16**, 1086–1091 (2021).
13. Zheng, F. et al. Direct imaging of a zero-field target skyrmion and its polarity switch in a chiral magnetic nanodisk. *Phys. Rev. Lett.* **119**, 197205 (2017).
14. Zhang, X. et al. Control and manipulation of a magnetic skyrmionium in nanostructures. *Phys. Rev. B* **94**, 094420 (2016).
15. Finazzi, M. et al. Laser-induced magnetic nanostructures with tunable topological properties. *Phys. Rev. Lett.* **110**, 177205 (2013).
16. Shen, Y. et al. Optical skyrmions and other topological quasiparticles of light. *Nat. Photonics* **18**, 15–25 (2024).
17. Zhang, S. et al. Real-space observation of skyrmionium in a ferromagnet-magnetic topological insulator heterostructure. *Nano Lett.* **18**, 1057–1063 (2018).
18. Seidel, J. Nanoelectronics based on topological structures. *Nat. Mater.* **18**, 188–190 (2019).
19. Salahuddin, S. & Datta, S. Use of negative capacitance to provide voltage amplification for low power nanoscale devices. *Nano Lett.* **8**, 405–410 (2008).
20. Tang, Y. L. et al. Observation of a periodic array of flux-closure quadrants in strained ferroelectric $PbTiO_3$ films. *Science* **348**, 547–551 (2015).
21. Yadav, A. K. et al. Observation of polar vortices in oxide superlattices. *Nature* **530**, 198–201 (2016).
22. Geng, W. R. et al. Rhombohedral-orthorhombic ferroelectric morphotropic phase boundary associated with a polar vortex in $BiFeO_3$ films. *ACS Nano* **12**, 11098–11105 (2018).
23. Nahas, Y. et al. Inverse transition of labyrinthine domain patterns in ferroelectric thin films. *Nature* **577**, 47–51 (2020).
24. Das, S. et al. Observation of room-temperature polar skyrmions. *Nature* **568**, 368–372 (2019).
25. Wang, Y. J. et al. Polar meron lattice in strained oxide ferroelectrics. *Nat. Mater.* **19**, 881–886 (2020).
26. Khalyavin, D. D. et al. Emergent helical texture of electric dipoles. *Science* **369**, 680–684 (2020).
27. Rusu, D. et al. Ferroelectric incommensurate spin crystals. *Nature* **602**, 240–244 (2022).
28. Gong, F. H. et al. Atomic mapping of periodic dipole waves in ferroelectric oxide. *Sci. Adv.* **7**, eabg5503 (2021).
29. Ma, J. et al. Controllable conductive readout in self-assembled, topologically confined ferroelectric domain walls. *Nat. Nanotechnol.* **13**, 947–952 (2018).
30. Geng, W. R. et al. Dipolar wavevector interference induces a polar skyrmion lattice in strained $BiFeO_3$ films. *Nat. Nanotechnol.* https://doi.org/10.1038/s41565-024-01845-5 (2025).
31. Yadav, A. K. et al. Spatially resolved steady-state negative capacitance. *Nature* **565**, 468–471 (2019).
32. Kim, K. T. et al. Chiral structures of electric polarization vectors quantified by X-ray resonant scattering. *Nat. Commun.* **13** (2022).
33. Li, Q. et al. Subterahertz collective dynamics of polar vortices. *Nature* **592**, 376–380 (2021).
34. Tong, P. R. et al. Thermal triggering for multi-state switching of polar topologies. *Nat. Phys.* **17** https://doi.org/10.1038/s41567-024-02729-0 (2025).

35. Geng, W. R. et al. Atomic-scale tunable flexoelectric couplings in oxide multiferroics. *Nano Lett.* **21**, 9601–9608 (2021).
36. Geng, W. R. et al. Magneto-electric-optical coupling in multiferroic $BiFeO_3$-based films. *Adv. Mater.* **34**, e2106396 (2022).
37. Liu, Z. et al. In-plane charged domain walls with memristive behaviour in a ferroelectric film. *Nature* **613**, 656–661 (2023).
38. Li, Z. et al. High-density array of ferroelectric nanodots with robust and reversibly switchable topological domain states. *Sci. Adv.* **3**, e1700919 (2017).
39. Nelson, C. T. et al. Spontaneous vortex nanodomain arrays at ferroelectric heterointerfaces. *Nano Lett.* **11**, 828–834 (2011).
40. Govinden, V. et al. Ferroelectric solitons crafted in epitaxial bismuth ferrite superlattices. *Nat. Commun.* **14**, 4178 (2023).
41. Han, M.-J. et al. Shape and surface charge modulation of topological domains in oxide multiferroics. *J. Phys. Chem. C.* **123**, 2557–2564 (2019).
42. Han, M. J. et al. Charged domain wall modulation of resistive switching with large ON/OFF ratios in high density $BiFeO_3$ nano-islands. Acta Mater. **187**, 12–18 (2020).
43. Maurice, V. et al. Self-assembling of atomic vacancies at an oxide/intermetallic alloy interface. *Nat. Mater.* **3**, 687–691 (2004).
44. Crosby, L. et al. Wulff shape of strontium titanate nanocuboids. *Surf. Sci.* **632**, L22–L25 (2015).
45. Geng, W. R. et al. Unveiling the pinning behavior of charged domain walls in $BiFeO_3$ thin films via vacancy defects. *Acta Mater.* **186**, 68–76 (2020).
46. Li, L. et al. Defect-induced hedgehog polarization states in multiferroics. *Phys. Rev. Lett.* **120**, 137602 (2018).
47. Higgins, M. et al. Non-invasive determination of optical lever sensitivity in atomic force microscopy. *Rev. Sci. Instrum.* **77**, 013701 (2006).
48. Anthony, S. M. & Granick, S. Image analysis with rapid and accurate two-dimensional Gaussian fitting. *Langmuir* **25**, 8152–8160 (2009).
49. Chen, L. Q. Phase-field method of phase transitions/domain structures in ferroelectric thin films: a review. *J. Am. Ceram. Soc.* **91**, 1835–1844 (2008).
50. Li, Y. et al. Effect of substrate constraint on the stability and evolution of ferroelectric domain structures in thin films. *Acta Mater.* **50**, 395–411 (2002).
51. Xue, F. et al. Orientations of low-energy domain walls in perovskites with oxygen octahedral tilts. *Phys. Rev. B* **90**, 220101 (2014).
52. Chen, L. Q. & Shen, J. Applications of semi-implicit Fourier-spectral method to phase field equations. *Comput. Phys. Commun.* **108**, 147–158 (1998).

Acknowledgements

This work is supported by National Natural Science Foundation of China (No. 52201018 (W.R.G.), No. 51971223 (Y.L.Z.), No. 51922100 (Y.L.T.), No. 92166104 (Z.H.), No. U21A2067 (Y.W.)), Guangdong Basic and Applied Basic Research Foundation (2021A1515110291 (W.R.G.), 2023A1515012796 (W.R.G.)), Guangdong Provincial Quantum Science Strategic Initiative (GDZX2202001, GDZX2302001, GDZX2402001 (X.L.M.)), the Open Fund of the Microscopy Science and Technology, Songshan Lake Science City (202401202 (W.R.G.)), the Key Research Program of Frontier Sciences CAS (QYZDJ-SSW-JSC010 (X.L.M.)) and Shenyang National Laboratory for Materials Science (L2019R06 (X.L.M.), L2019R08 (Y.L.Z.), L2019F01 (Y.L.T.), L2019F13 (Y.J.W.)), Y.L.T. acknowledges the Scientific Instrument Developing Project of CAS (YJKYYQ20200066), and the Youth Innovation Promotion Association of CAS (Y202048). Z. H. acknowledges a financial support by the Fundamental Research Funds for the Central Universities (2023QZJH13). Y.J.W. acknowledges the Youth Innovation Promotion Association CAS (No. 2021187). The phase-field simulation was performed on the MoFang III cluster on Shanghai Supercomputing Center (SSC). X.G. is supported by the National Natural Science Foundation of China (No. 52202151) and China Postdoctoral Science Foundation (No. 2022M722715).

Author contributions

W.R.G. and X.G. contributed equally to this work. X.L.M. conceived the project on the architecture of quantum materials modulated by ferroelectric polarizations; W.R.G., Y.L.Z. and X.L.M. designed the sample structures and subsequent experiments. W.R.G. performed the thin-film growth and PFM observations. W.R.G., Y.L.T. performed the TEM and STEM observations. X.G., D.M., Y.W. and Z.H. performed the phase-field simulations. D.M. and Y.J.W. carried out digital analysis of the STEM data. All authors participated in discussion and interpretation of the data.

Competing interests

The authors declare no competing interests.

Additional information

Supplementary information The online version contains supplementary material available at https://doi.org/10.1038/s41467-025-58008-w.

Correspondence and requests for materials should be addressed to Zijian Hong or Xiu-Liang Ma.

Peer review information *Nature Communications* thanks Congbing Tan, and the other, anonymous, reviewer(s) for their contribution to the peer review of this work. A peer review file is available.

RESEARCH ARTICLE

ADVANCED FUNCTIONAL MATERIALS
www.afm-journal.de

Interfacial Manipulation of Polar Topologies in Oxide Ferroelectric Films

Yan-Peng Feng, Yu-Jia Wang, Yun-Long Tang, Yin-Lian Zhu, and Xiu-Liang Ma**

Topological polar structures hold significant potential for high-density memories and low-power electronic devices. Interfacial engineering offers a promising route to manipulate topological polar structures in ferroelectric heterostructures, yet the underlying mechanisms remain elusive. Here, deterministic manipulation of topological polar Bloch points and merons in epitaxial $PbTiO_3$ (PTO) films are demonstrated via designing symmetric and asymmetric interfaces. By integrating $SrRuO_3$ (SRO) and $SmScO_3$ (SSO) layers, it is shown that symmetric PTO/SSO interfaces effectively stabilize polar Bloch points in PTO/SSO bilayers and $(PTO)_{13}/(SSO)_9$ superlattices whereas asymmetric configurations (e.g., SRO/PTO, SRO/PTO/SSO) favor the formation of polar merons, which are visualized by aberration-corrected scanning transmission electron microscopy. Phase-field simulations reveal that the stabilization of Bloch points and merons is governed by the competition between elastic and electrostatic energies. The built-in electric field and interfacial symmetry coupling with topological textures are identified as critical factors in modulating topological stability. Piezoresponse force microscopy measurements demonstrate that the presence of polar Bloch points enhances the piezoelectric response of the ferroelectric films. These findings illustrate interfacial engineering as a key strategy for designing and stabilizing nanoscale polar topologies, which may promote their potential applications in future electronic devices.

1. Introduction

Recently, the discovery of topological polar structures, including flux-closures, vortices, skyrmions, merons, and Bloch points, in ferroelectric systems has opened new frontiers for exploring emergent phenomena and advanced devices.[1–10] These topological states, which involve non-trivial configurations of electric polarization, exhibit remarkable features such as nanoscale sizes,[11] topological protection,[12] metallic conduction,[13] and negative capacitance,[14] and ultrafast collective polarization dynamics,[15] which prompts them promising candidates for next-generation high-density nonvolatile memory and ultra-low-power electronics.[16–18] However, the deterministic creation, stabilization, and manipulation of these topological structures remain significant challenges, particularly in practical device architectures where interfacial effects is paramount.[19–23]

The role of interfacial engineering in manipulating ferroelectric polarization has recently attracted much attention. Interfaces in heterostructures, multilayers or superlattices introduce symmetry breaking, strain gradients, and charge redistribution, which can dramatically alter the local energy landscape. As a result, the ferroelectric polarization might be enhanced, suppressed or rotated near heterogeneous interfaces.[24–26] The heterogenous interfaces not only influence the overall polarization state but also play a crucial role in the formation and stabilization of topological polar structures. Some researchers have reported that the nontrivial polar structures, including polar flux-closures, vortices, polar

---

Y.-P. Feng, Y.-L. Zhu, X.-L. Ma
Bay Area Center for Electron Microscopy
Songshan Lake Materials Laboratory
Dongguan, Guangdong 523808, China
E-mail: zhuyinlian@sslab.org.cn; xlma@iphy.ac.cn

Y.-P. Feng, Y.-L. Zhu, X.-L. Ma
Quantum Science Center of Guangdong-HongKong-Macao Greater Bay Area
Shenzhen, China

Y.-J. Wang, Y.-L. Tang
Shenyang National Laboratory for Materials Science, Institute of Metal Research
Chinese Academy of Sciences
Wenhua Road 72, Shenyang 110016, China

Y.-L. Zhu
School of Materials Science and Engineering
Hunan University of Science and Technology
Xiangtan 411201, China

X.-L. Ma
Institute of Physics
Chinese Academy of Sciences
Beijing 100190, China

X.-L. Ma
State Key Lab of Advanced Processing and Recycling on Non-ferrous Metals
Lanzhou University of Technology
Lanzhou 730050, China

The ORCID identification number(s) for the author(s) of this article can be found under https://doi.org/10.1002/adfm.202510402

DOI: 10.1002/adfm.202510402

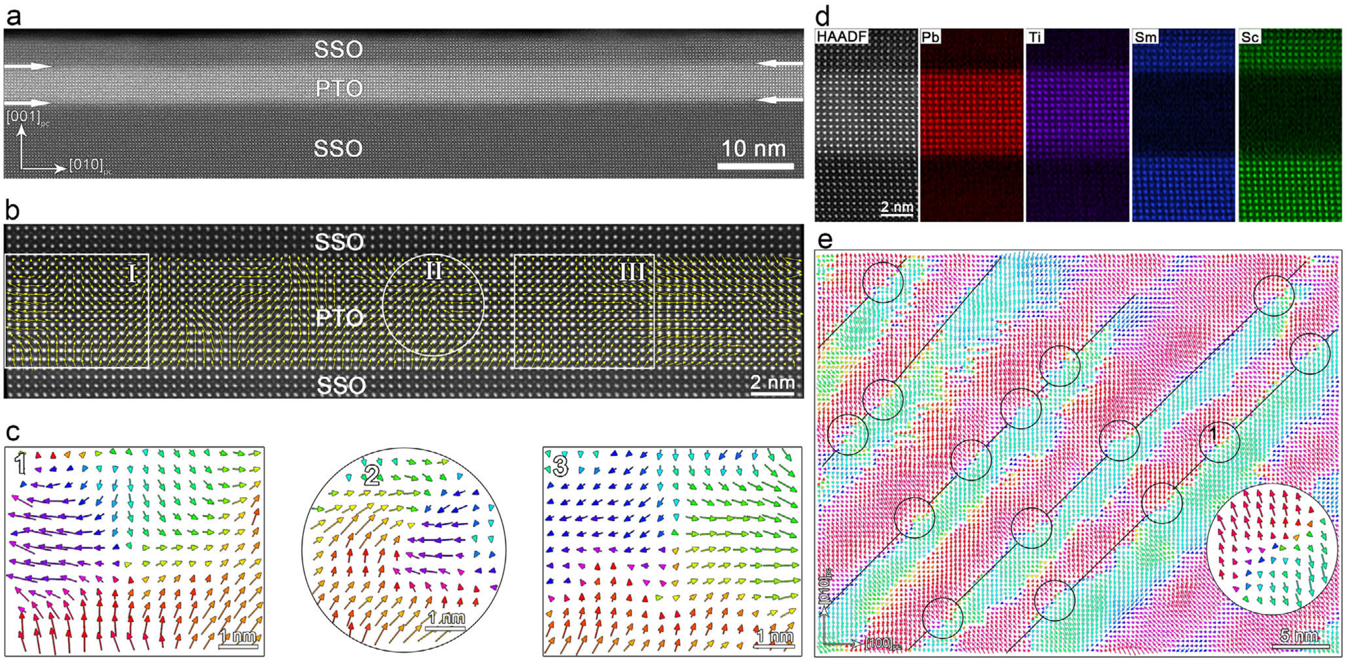

Figure 1. Observation of polar Bloch points in PTO/SSO bilayers. a) The low-magnification cross-sectional HAADF-STEM image of PTO/SSO bilayer film. b) Superposition of reversed Ti-displacement vectors ($-\delta_{Ti}$) and atomic-resolved HAADF-STEM image. The $-\delta_{Ti}$ vectors of PTO unit cells were shown as yellow arrows. c) Magnified $-\delta_{Ti}$ vector maps showing three typical polarization patterns marked as "1"-"3" in the thin film corresponding to three boxes/circles labeled as "I"-"III" in (b), respectively. d) Atomic-resolved HAADF-STEM image and EDS mapping of the thin film showing the sharp SSO/PTO interfaces. e) The $-\delta_{Ti}$ vector map based on atomic-resolved planar-view HAADF-STEM image, showing the divergent polarization patterns (black circles) at tail-to-tail domain walls (black lines). The arrows with different colors denote the polarization directions of PTO unit cells. The inset of (e) is the magnified $-\delta_{Ti}$ vector map of a typical divergent polarization pattern marked by "1".

waves and skyrmions, can be stabilized by inserting an insulating layer between two ferroelectric layers in ferroelectric $PbTiO_3/SrTiO_3$ (PTO/STO) multilayers or superlattices.[1–3,6,9] However, alternative perspectives have been presented by other researchers. For instance, Li et al. demonstrated that the polar flux-closures can still be maintained in PTO layers when covered by the same electrodes or insulators, but these structures break down and transform into *a*/*c* domains when the PTO layer is clamped by different films.[27] On the other hand, Hadjimichael et al. revealed that a stable supercrystal phase comprising a three-dimensional ordering of nanoscale flux-closures can be engineered in $PbTiO_3/SrRuO_3$ (PTO/SRO) ferroelectric–metal superlattices.[28] Moreover, Peters et al. reported that the polar vortices can exsit under asymmetric Co/$PbTiO_3$/(La,Sr)MnO_3 ferroelectric tunnel junctions.[29] These seemingly controversial findings underscore the complex interplay between interfacial design and polarization behavior, offering a pathway to manipulate polar topological states via interfacial engineering.

In this work, we investigate the role of interfacial engineering in controlling topological polar structures within epitaxial PTO heterostructures. By designing symmetric and asymmetric interfaces with the integration of SRO and SSO layers, we demonstrate the polar Bloch points and merons can be controllably manipulated. Specifically, the symmetric SSO/PTO interfaces can easily stabilize the polar Bloch point in PTO/SSO bilayer and $(PTO)_{13}/(SSO)_9$ superlattices, whereas the asymmetric interfaces easily favor the formation of polar merons in SRO/PTO and SRO/PTO/SSO film systems. The phase-field simulations reveal that the built-in electric field plays an important role in the formation of different topological domain structures. Further energy analysis indicates that the competition between elastic and electrostatic energies influences the stabilization of Bloch points and merons. Additionally, the coupling mechanism between interfacial symmetry and topological textures for manipulating topological polar structures was systematically discussed, which provides insights into how interfacial engineering can be leveraged to manipulate topological polar structures.

2. Results and Discussion

In our prior work, the emergence of polar Bloch points was identified within SRO/PTO/SRO trilayer thin films epitaxially grown on orthorhombic (110)-oriented SSO substrates, which underscore the pivotal influence of the short-circuit and symmetric boundary conditions on the stabilization of polar Bloch points.[5] To further investigate the interfacial effects on the formation of polar Bloch points, the PTO thin film with thickness of about 5 nm (13 unit cells) was epitaxially grown on an orthorhombic (110)-oriented SSO substrate via pulsed laser deposition (PLD). Subsequently, an SSO layer with 3.5 nm (9 unit cells) was covered on the PTO film to create symmetric SSO/PTO interfaces under open-circuit boundary conditions (details of film deposition are provided in Experimental Section). **Figure 1a** shows a low-magnification cross-sectional high-angle annular dark-field scanning transmission electron microscopy (HAADF-STEM) image, displaying the smooth SSO/PTO interfaces, as marked by white arrows. The planar-view transmission electron microscopy (TEM) image (Figure S2, Supporting Information) exhibits characteristic strip domains, which resemble a_1/a_2 domain configurations. Figure 1b displays a superposition of reversed Ti-displacement vectors ($-\boldsymbol{\delta}_{\mathrm{Ti}}$, marked by yellow arrows) and the atomic-resolved HAADF-STEM image (the original image is provided in Figure S1, Supporting Information), where the $-\boldsymbol{\delta}_{\mathrm{Ti}}$ vectors correspond to the local spontaneous polarization directions within PTO unit cells. To elucidate the polarization configuration in the PTO film, three typical regions labeled as "I"-"III" are magnified and displayed as "1"-"3" in Figure 1c, respectively. Regions "1" and "3" exhibit characteristic antivortex patterns, while region "2" displays a convergent pattern, with these patterns arranged in an alternating configuration. Atomic-resolution X-ray energy dispersive spectroscopy (EDS) mappings (Figure 1d) demonstrate the exceptional sharpness of both SSO/PTO interfaces, with no evidence of interfacial diffusion. The planar-view polarization configuration based on atomic-resolved planar-view HAADF-STEM image (the original one is provided in Figure S3, Supporting Information) was further analyzed and shown in Figure 1e. The high-resolution $-\boldsymbol{\delta}_{\mathrm{Ti}}$ vector map is displayed in Figure S4a (Supporting Information). The ordered stripe domains were identified in this PTO film, which features many"head-to-head" and "tail-to-tail" domain walls (DWs), marked by black and white arrows, respectively. Notably, each "tail-to-tail" DW (indicated by black solid lines in Figure 1e) contains multiple divergent polarization patterns (marked by black solid circles), forming approximate one-dimensional arrays. The inset of Figure 1e shows a magnified view (marked by "1") of a typical divergent configuration. Besides, convergent polarization patterns are predominantly observed at "head-to-head" DWs, also arranged in a one-dimensional array (Figure S4b, Supporting Information). These results indicate that the polar Bloch points could be stabilized in the PTO/SSO bilayers.

The $(\mathrm{PTO})_{13}/(\mathrm{SSO})_9$ superlattices were further grown on the orthorhombic (110)-oriented SSO substrates via PLD, where the subscripts of 13 and 9 denote the thickness of the PTO and SSO layers in unit cells (details of film deposition are provided in Experimental Section). A low-magnification cross-sectional HAADF-STEM image (**Figure 2**a) and EDS mappings (Figure S5a, Supporting Information) of the $(\mathrm{PTO})_{13}/(\mathrm{SSO})_9$ superlattice, acquired along the in-plane $[100]_{\mathrm{pc}}$ direction, reveal the uniformity of the PTO and SSO layers. The atomic-resolved HAADF-STEM image (Figure 2b) and EDS mappings (Figure S5b, Supporting Information) further confirm the sharp and coherent interfaces (labeled as yellow dashed lines) in $(\mathrm{PTO})_{13}/(\mathrm{SSO})_9$ superlattice. The polarization configuration (Figure 2c) was analyzed by extracting the $-\boldsymbol{\delta}_{\mathrm{Ti}}$ vector map from the region in Figure 2b. The original high-resolution HAADF-STEM image and the high-resolution polarization map of Figure 2c are provided as Figures S6 and S7 (Supporting Information), respectively. The convergent and antivortex polarization patterns are distinctly observed within individual PTO layers, as labeled by black solid circles and rectangle boxes, respectively. Figure 2d,f are two magnified HAADF-STEM images of the regions marked by white rectangle boxes labeled as "1" and "2", respectively. The yellow and red circles denote the Pb and Ti atom columns, respectively. The yellow arrows point to the polarization directions of PTO unit cells. Figure 2e,g are two polarization maps corresponding to the area of Figure 2d,f, respectively, which exhibits the convergent and antivortex polarization patterns. These results reveal that the polar Bloch points can be retained in each PTO layer under symmetric SSO/PTO interfacial conditions.

The SRO/PTO bilayer was subsequently grown (110)-oriented SSO substrate to establish an asymmetric boundary condition of top PTO/vacuum and bottom SRO/PTO interfaces. **Figure 3**a presents the cross-sectional HAADF-STEM image of the SRO/PTO bilayer film, where both the PTO and SRO layers exhibit uniform thicknesses of approximately 5 nm. The in-plane lattice strain, as depicted in Figure 3b, was extracted by geometric phase analysis (GPA), which reveals an alternating arrangement of two distinct trapezoidal domain patterns. Those are Type-I domains (green regions) with upward-opening configurations and Type-II domains (red regions) with downward-opening configurations. Figure 3c displays an atomic-resolution HAADF-STEM image, highlighting the sharp and smooth interface between the SRO and PTO layers. A magnified view of the region marked by a dashed rectangle in Figure 3c, which contains both Type-I and Type-II domains, is shown in Figure 3d. In this image, yellow and red circles denote Pb and Ti atoms, respectively, while yellow arrows indicate the polarization direction of the PTO unit cells. The trapezoidal domains exhibit *c* domains with out-of-plane polarization at their centers and *a* domains with in-plane polarization along their edges. Figure 3e illustrates the reversed Ti-displacement vectors ($-\boldsymbol{\delta}_{\mathrm{Ti}}$) corresponding to the area shown in Figure 3d, representing the directions of local spontaneous polarization (**Ps**). The Type-I domain exhibits a divergent polarization pattern, while the Type-II domain displays a convergent polarization configuration, both of which are characteristic of merons as previously reported.[4] Additionally, the in-plane lattice parameter mapping (Figure 3f) corresponding to the same region as Figure 3d further corroborates the alternating trapezoidal patterns, consistent with the in-plane strain mapping shown in Figure 3b.

The SSO layer was further covered on top of SRO/PTO bilayers to create an additional asymmetric boundary condition with top PTO/SSO and bottom SRO/PTO interfaces. **Figure 4**a shows the cross-sectional HAADF-STEM image of SRO/PTO/SSO trilayers, where the thickness of the SSO layer is about 3 nm. Figure 4b presents the in-plane lattice strain mapping corresponding to the region of Figure 4a, revealing the trapezoidal and inclined stripe domains within the PTO layer. Two specific regions labeled as ′1-2″ in Figure 4a were magnified and shown in Figure 4c,d, respectively. Similarly, yellow and red circles denote Pb and Ti atoms, respectively, while yellow arrows indicate the polarization direction of the PTO unit cells in these images. Figure 4e,f display the polarization mappings of the regions in Figure 4c,d, respectively. It is seen that the trapezoidal domain exhibits a divergent polarization pattern, which is characteristic of a polar meron as previously.[4] The inclined stripe domain features a typical 90° *a*/*c* domains. Besides, the trapezoid and inclined stripe (Figure 4g,h) were further illustrated by extracting lattice parameter corresponding to areas of Figure 4c,d, respectively.

The phase-field simulations were performed to clarify the effect of interfaces on the formation of polar Bloch points and merons. Three distinct models were developed in simulations to reproduce experimental observations. The work function

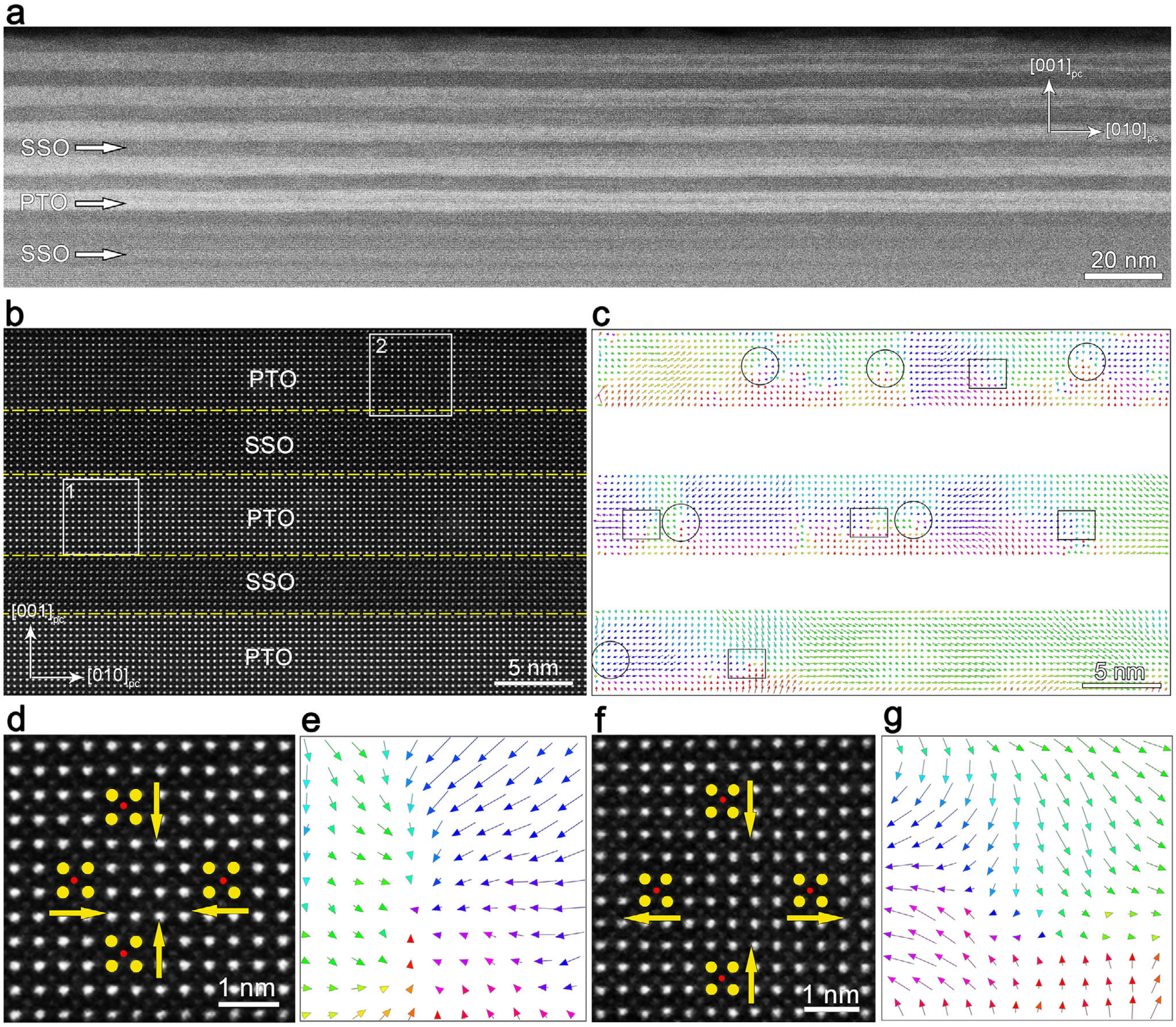

Figure 2. Observation of polar Bloch points in the $(PTO)_{13}/(SSO)_9$ superlattice. a) Low-magnification HAADF-STEM image of the cross-sectional $(PTO)_{13}/(SSO)_9$ superlattice viewed along the [100] direction of PTO. The bright and weak layers are PTO and SSO, respectively. b) Atomic-resolved HAADF-STEM image of the cross-sectional $(PTO)_{13}/(SSO)_9$ superlattice viewed along the [100] direction of PTO. The yellow dashed lines denote the PTO/SSO interfaces. c) The $-\boldsymbol{\delta}_{\mathbf{Ti}}$ vector map corresponding to the area of Figure 2b. The black solid circles and rectangle boxes indicate the convergent and antivortex polarization patterns, respectively. d) and f) The magnified HAADF-STEM images of the areas marked by white rectangle boxes labeled as "1" and "2", respectively. e) and g) The polarization mappings corresponding to the areas of (d) and (f), respectively. The arrows with different colors in (c), (e) and (g) denote the polarization directions of PTO unit cells.

disparity among SSO, SRO, and PTO may generate a built-in electric field within the PTO layer, inducing the polarization vectors away from the SSO/PTO interface and toward the SRO/PTO interface (Figures 1 and 3).[27,30–33] Based on this mechanism, Model 1 employs a convergent electric field in the PTO layer (**Figure** 5a), whose magnitude is comparable to our previous work but reversed in direction.[5] Model 2 incorporates a downward electric field with the magnitude of 20 MV/m to simulate PTO films grown on SRO electrodes (Figure 5b). Model 3 simulates a PTO layer that is sandwiched between top SSO and bottom SRO layers. As shown in Figure 4, the polarization vectors in the *c* domains of the PTO film point away the SSO/PTO interface toward the SRO/PTO interface, which indicates that the built-in electric fields are also downward. Consequently, a downward electric field of 20 MV/m is applied in this model, as shown in Figure 5c. The domain structures in the PTO film for three models are initialized as meron lattice and the optimized domain patterns are presented in Figure 5d–l. The 3D domain patterns (Figure 5d–f) reveal that the *c* domain pairs appear in the first model and the funnel-shaped *c* domains exist in the latter two models, which indicates that Bloch points emerge in the first model and merons form in the second and third models.

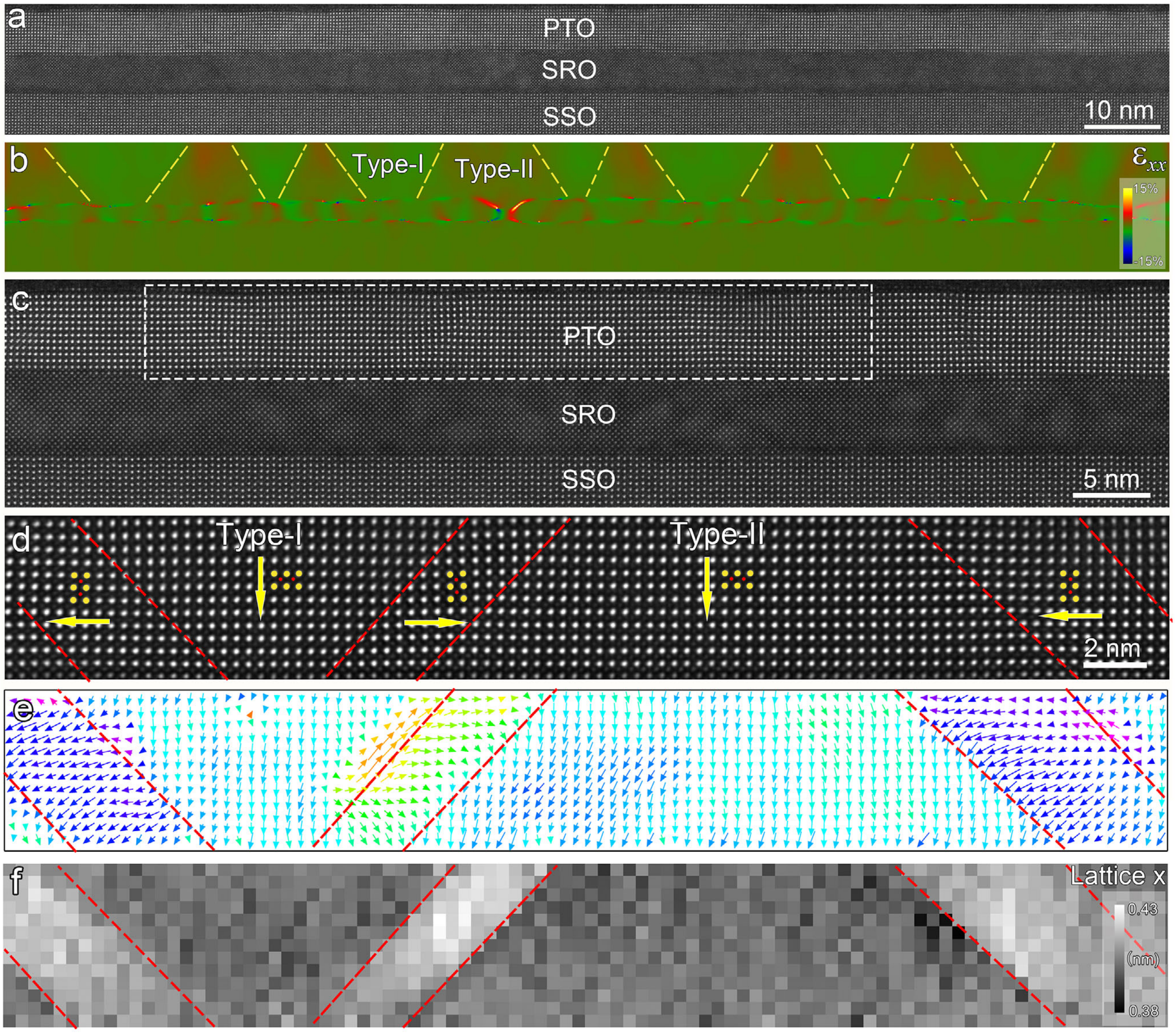

Figure 3. Observation of polar merons in the SRO/PTO bilayers grown on a SSO substrate. a) Cross-sectional HAADF-STEM image of SRO/PTO bilayers viewed along the [100] direction of PTO. b) In-plane lattice strain mapping (ε_{xx}) corresponding to the area of (a). c) Atomic-resolved HAADF-STEM image of the SRO/PTO bilayers. d) The magnified HAADF-STEM image corresponding to the area labeled as dashed rectangle of (c). Yellow and red circles denote Pb and Ti atoms, respectively. Yellow arrows indicate the polarization direction of the PTO unit cells. e) The $-\delta_{\mathrm{Ti}}$ vector mapping corresponding to the area of (d). f) In-plane lattice parameter mapping corresponding to the area of (e).

Comparing Figure 5e,f, it is found that the *c* domains in Figure 5e are generally larger than those in Figure 5f. It could be attributed to this fact that the top SSO further clamps the PTO film, which impedes the formation of *c* domains. This interpretation aligns with the reduced *c* domain fraction observed in Figure 4 compared to Figure 3. Figure 5g–i show the horizontal cross-sections in the middle of the PTO films for the three models. The minimal *c* domains are shown in Figure 5g since the *c* domains of the Bloch points mainly locate in the top and bottom parts of the PTO film. In contrast, prominent *c* domains exist in the middle of PTO films under second and third models, which are located at polar merons. Figure 5j–l show three-dimensional polarization structures corresponding to the three regions marked by dashed boxes in Figure 5g–i, respectively. It is noted that the Bloch point (Figure 5j) exhibits divergent in-plane and convergent out-of-plane configurations, while both merons (Figure 5k,l) display down-divergent characteristics. These simulated polarization topologies show consistency with experimental findings. Further comparison of energies presented in Table S1 (Supporting Information) reveals that the primary differences arise from electrostatic and elastic energies. Model 1 exhibits the lowest electrostatic energy, which could be attributed to the effect of a convergent electric field. In contrast, Model 2 shows the highest elastic energy, which is likely due to the presence of large *c* domains in the film system. The elastic energy is reduced in Model 3 due to the decrease of *c* domains

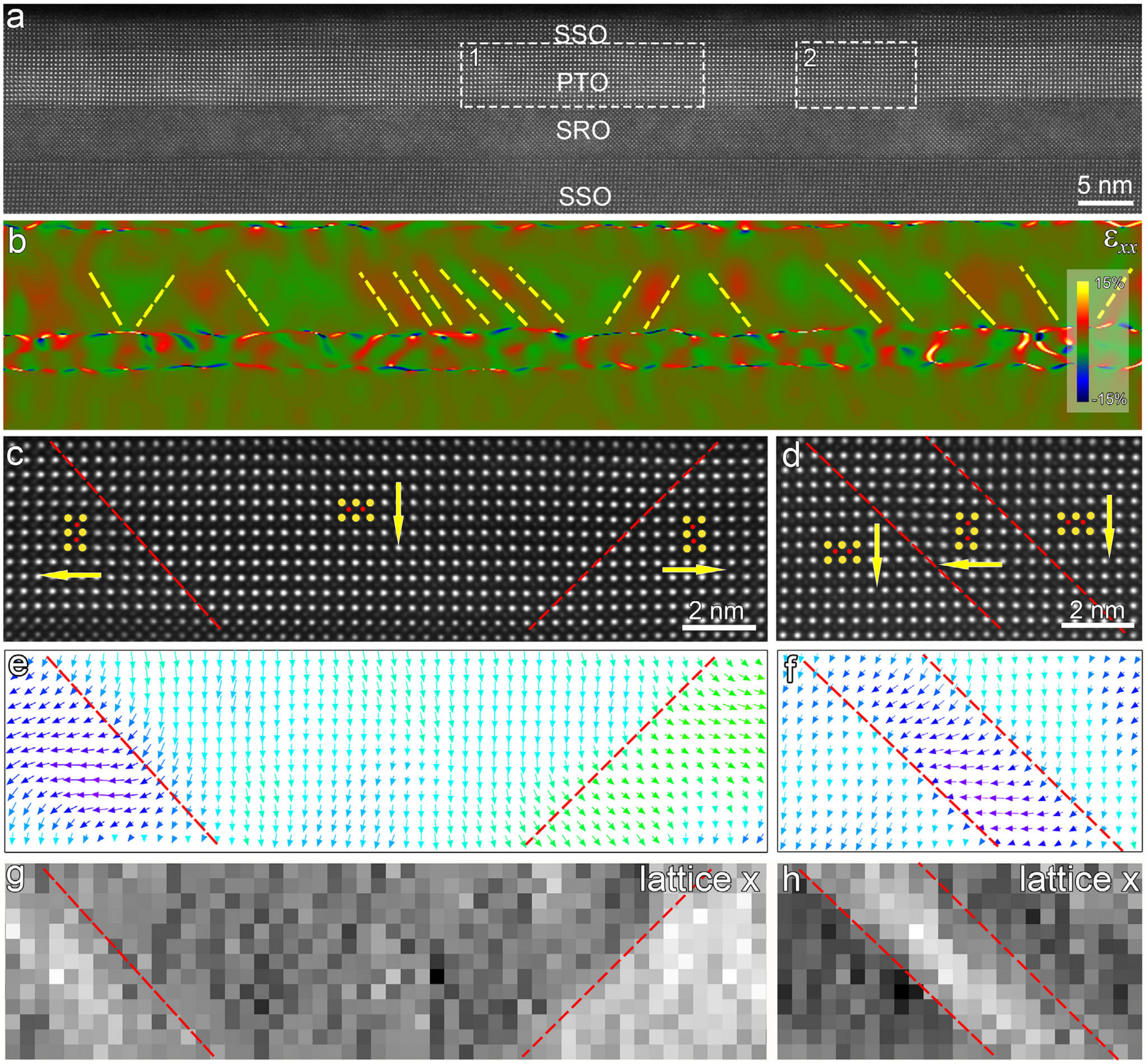

Figure 4. Observation of polar merons and *a*/*c* domains in the SRO/PTO/SSO trilayers grown on a SSO substrate. a) Cross-sectional HAADF-STEM image of SRO/PTO/SSO trilayers taken along the [100] direction of PTO. b) In-plane lattice strain mapping (ε_{xx}) corresponding to the area of (a). c,d) Magnified HAADF-STEM images of the SRO/PTO/SSO trilayers corresponding to the areas marked by dashed rectangles "1-2" in (a), respectively. Yellow and red circles denote Pb and Ti atoms, respectively. Yellow arrows indicate the polarization direction of the PTO unit cells. e, f) The $-\delta_{\mathrm{Ti}}$ vector mappings corresponding to the area of (c–d), respectively. g,h) In-plane lattice parameter mappings corresponding to the area of (c,d), respectively.

when covered with a SSO layer. These results demonstrate that the stabilization of Bloch points and merons is mainly governed by the competition between elastic energy and electrostatic energy.

The controllable formation of polar topologies in ferroelectric films is critical in nanoscale ferroelectrics. Generally, the stabilization of topological polar structures depends on the competition of the bulk, elastic, electrostatic and gradient energies of the system.[2,4,5] The strain engineering and electrical boundary conditions have been established as conventional strategies for manipulating polar topologies.[1–4,34–36] Nevertheless, our systematic investigations demonstrate that interfacial symmetry could serve as a distinct approach to govern topological polar structures. In the prior work, polar Bloch points were stabilized in short-circuited SRO/PTO/SRO heterostructures,[5] whereas polar meron lattices were observed in ultrathin PTO monolayers grown on SSO substrates.[4] However, in this work, by combining experimental observations and phase-field simulations we demonstrate that polar Bloch points can also be stabilized in symmetric SSO/PTO/SSO architectures, while merons persist in asymmetric systems such as SRO/PTO and SRO/PTO/SSO films. These findings indicate that the decisive factor for

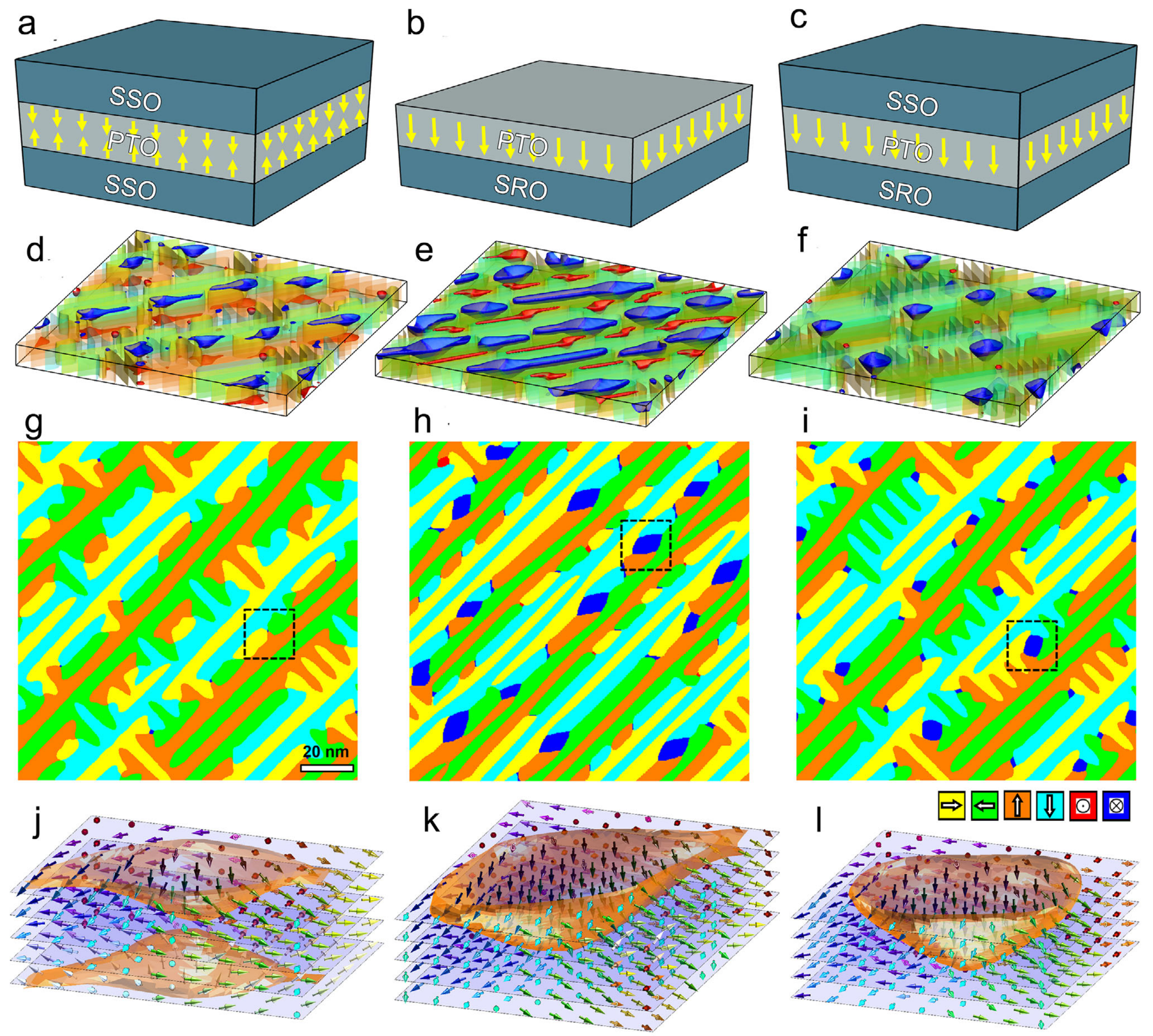

Figure 5. The phase-field simulations of the symmetric and asymmetric boundary conditions. a–c) the schematic diagrams of different models. (a) The PTO film sandwiched by two SSO layers or under the symmetric boundary condition. (b) The PTO film grown on the SRO electrode. (c) The PTO film sandwiched by SSO and SRO. The yellow arrows represent the directions of local electric fields. d–f) The three-dimensional domain structures for the three models. g–i) The horizontal cross-sections at the middle of the PTO films for the three models. j–l) Three-dimensional polarization structures for the three regions marked by dashed boxes in (g–i). The brown semitransparent surfaces are the isosurfaces of $|P_z| = 0.5\ P_s$. The spacings between two adjacent vectors in the in-plane and out-of-plane directions are 2 and 1 nm, respectively.

manipulating polar Bloch points and merons could be not the electrical boundary condition, but the interfacial symmetry. Specifically, symmetric interfaces thermodynamically stabilize polar Bloch points, whereas asymmetric interfaces preferentially host merons textures.

The polar Bloch points exhibit mirror symmetric out-of-plane polarization configurations (Figure 1c), while polar merons display asymmetrically vertical polarization patterns with alternating divergent or convergent patterns (Figure 3e). This symmetry matching mechanics could imply that the symmetric interfaces minimize depolarization energy through charge compensation at both interfaces to favor symmetric topological states. In contrast, asymmetric interfaces could induce unidirectional screening that can stabilize non-symmetric topological textures. This phenomenon is also corroborated by previous work. For instance, symmetric topological polar structures along the out-of-plane direction, including flux-closures, vortices, and skyrmions have been predominantly observed in symmetric PTO/STO multilayers and superlattices,[1–3] whereas the central domain structures with asymmetric out-of-plane polarizations typically emerge in BFO monolayer films with asymmetric interfacial constraints.[12,13,37–39]

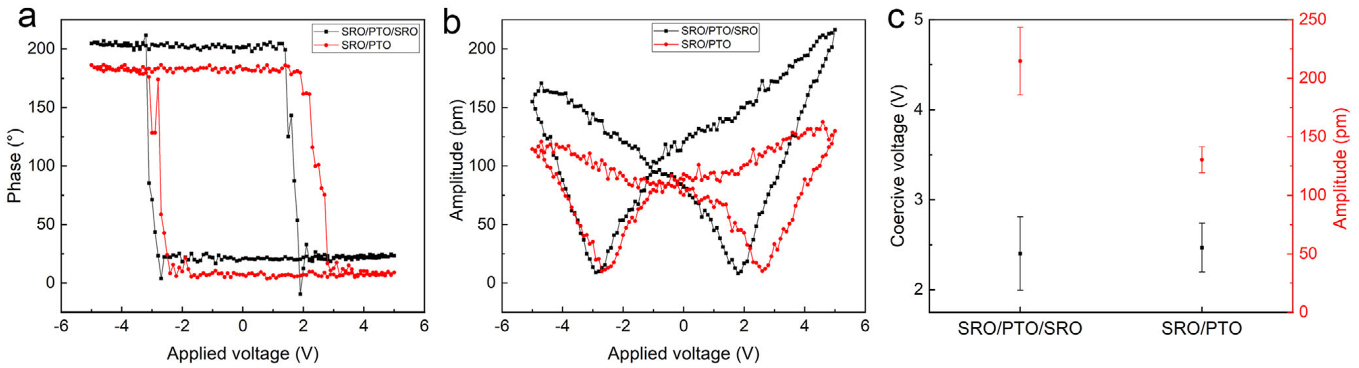

Figure 6. The local PFM hysteresis loop measurements of the SRO/PTO/SRO and SRO/PTO films. a) Phase hysteresis loops and b) amplitude hysteresis loops. c) Statistical results of coercive voltage and piezoresponse amplitude of the SRO/PTO/SRO and SRO/PTO films.

The interfacial symmetry and polarization coupling mechanism revealed here provides a universal framework for manipulating topological polar structures through interfacial engineering. The rational design of interfacial symmetry in ferroelectric heterostructures opens new avenues for manipulating polar topological states. Our findings of interfacial manipulation on polar topologies enable three peculiar capabilities. First, the transformation from polar Bloch points to merons can be achieved through intentional symmetry breaking at engineered interfaces. Second, vertical integration of diverse polar topologies becomes feasible through multilayer architectures combining alternating symmetric and asymmetric interfaces, which highlights the potential for three-dimensional topological multistate. Third, by strategically combining symmetric/asymmetric interfaces with strain engineering, more new topological polar structures could be created in oxide ferroelectric films. These advances position ferroelectric heterostructures as viable platforms for next-generation high-density memories based on polar topologies.

To further elucidate how the polar Bloch points and merons influence the physical properties of ferroelectric films, we have performed piezoresponse force microscopy (PFM) measurements. Local PFM hysteresis loops were acquired using the dual AC resonance tracking (DART) mode, which effectively minimizes topographic crosstalk and improves the signal-to-noise (S/N) ratio.[40] Due to the absence of a bottom electrode in the PTO/SSO bilayers, a relatively high voltage (~30 V) was required to induce polarization switching (Figure S8, Supporting Information). Additionally, in the SRO/PTO/SSO film (Figure 4), the coexistence of merons and *a*/*c* domains likely contributes to the piezoelectric response in a manner that extends beyond the intrinsic effects of the topological structures. Therefore, to directly compare the contributions of polar Bloch points and merons, we measured local PFM hysteresis loops for two similar heterostructures. The one is the previously reported SRO/PTO/SRO trilayer, which hosts polar Bloch point arrays,[5] and the other is the present SRO/PTO bilayer, characterized by periodic meron structures (Figure 3). As shown in **Figure 6**a, both samples exhibit well-defined square-shaped phase hysteresis loops, indicating robust ferroelectric switching behavior.[41] The corresponding amplitude hysteresis loops (Figure 6b) display typical butterfly-like shapes. Critically, the SRO/PTO/SRO trilayer exhibits a significantly higher piezoresponse amplitude than the SRO/PTO bilayer, suggesting enhanced piezoelectric properties. To quantitatively assess the differences in ferroelectric switching and piezoelectric response, we performed statistical analyses of the coercive voltage (E_c) and the maximum piezoresponse amplitude (Figure 6c). The statistical results were summarized in Table S2 (Supporting Information). While the coercive voltages are comparable between the two films, the average piezoresponse amplitude of the SRO/PTO/SRO trilayer is approximately 65% higher than that of the SRO/PTO bilayer. This enhanced piezoresponse in the trilayer film may be attributed to the following two primary factors. On one hand, experimental observations and phase-field simulations reveal that the polar Bloch point has a smaller size, leading to the higher density of topological domains within the SRO/PTO/SRO film,[5] which could strengthen the piezoelectric response. Previous studies have also reported that the high density of ferroelectric domains can strengthen the response to external electric fields.[42,43] On the other hand, the spherical polarization configuration of polar Bloch points allows for polarization components in all spatial directions, enabling more flexible and efficient responses to external electric fields. Our results highlight the critical role of engineered topological structures in enhancing electromechanical properties and suggest a promising strategy for the design of high-performance piezoelectric devices.

3. Conclusion

In summary, we demonstrated the interfacial manipulation on polar Bloch points and merons in ferroelectric PTO films. A series of PTO heterostructures and superlattices with symmetric and asymmetric SSO or SRO layers were deposited on (110)-oriented SSO substrates by PLD method. Aberration-corrected transmission electron microscopy demonstrates that the polar Bloch points are easily stabilized in PTO/SSO bilayer and $(PTO)_{13}/(SSO)_9$ superlattices with symmetric SSO/PTO interfaces, whereas they will transform into polar merons and *a*/*c* domains in SRO/PTO and SRO/PTO/SSO film systems with asymmetric interfaces. Phase-field simulations reveal that the built-in electric field in PTO layer plays an important role in the formation of different topological polar structures. Furthermore, it is pointed out that the formation of polar Bloch points and merons is mainly dominated by the competition between elastic and electrostatic energies. PFM measurements demonstrate that the formation polar Bloch points can enhance the piezoelectric responses of ferroelectric films. Our results illustrate that interface engineering can be used to manipulate topological polar structures. This study not only advances the understanding of interfacial manipulation on polar topologies but also paves the way for exploiting these exotic states in high-density memory, energy-efficient electronics and high-performance piezoelectric devices.

4. Experimental Section

Film Deposition: A series of ferroelectric film systems were deposited on orthorhombic (110)-oriented SSO single-crystal substrate by pulsed laser deposition (PLD), using the Coherent ComPex PRO 201 F KrF excimer laser ($\lambda = 248$ nm). The sintered PTO target with 3 mol% Pb enrichment and stoichiometric SSO and SRO targets were used to deposit PTO, SSO and SRO layers, respectively. Before film deposition, the SSO substrate was pre-heated to 800 °C and kept for 10 min to make the surface cleaning and then cooled down the temperature of film deposition. The PTO, SSO and SRO targets were pre-sputtered for 5 min to clean the target surfaces, respectively. During SRO deposition, the temperature of 680 °C, an oxygen pressure of 7 Pa, laser energy of 300 mJ, and repetition rate of 4 Hz were used while the parameters of PTO and SSO layers deposition were oxygen pressure of 10 Pa, laser energy of 350 mJ and repetition rate of 4 Hz. After deposition, the samples were annealed at 700 °C for 5 min in an oxygen pressure of 3×10^4 Pa, and then cooled down to room temperature with the cooling rate of 5 °C min^{-1}.

TEM Samples Preparation and HAADF-STEM Imaging: Cross-sectional samples for STEM observations were prepared through a traditional process involving gluing, grinding, dimpling and Ar ion milling using a Gatan Precision Ion Polishing System 695. The initial voltage of 4.5 kV and an angle of 7° were used for ion milling. Then, the voltage and angle were gradually reduced. The final voltage of 0.5 kV was used to reduce the damage by ion beam. The planar-view samples for STEM observations were specifically prepared by limiting ion milling from the substrate side to preserve the film structure.

Atomic-resolution HAADF-STEM imaging for cross-sectional and planar-view samples was conducted on an aberration-corrected scanning transmission electron microscope (Spectra 300 X-FEG microscope, ThermoFisher Scientific) equipped with CEOS double aberration (Cs) correctors and a monochromator, which was operated at 300 kV. The STEM Drift Corrected Frame Integration (DCFI) technique was used to minimize the sample drift when acquiring atomic-resolved HAADF-STEM images. The DCFI technique records successive original STEM images and integrates a high-quality STEM image via calculating and correcting the drift from cross correlation.[44] Each high-resolution HAADF-STEM image was acquired by integrating 20 sequential frames with the dwell time of 200 ns using Velox software (ThermoFisher Scientific), which ensures a high signal-to-noise ratio for precise atomic-scale polarization analysis.

Strain Analysis and Determining the Position of Atom Columns: The large area strain field in HAADF-STEM images were deduced by Geometric Phase Analysis (GPA), which was carried out by Gatan Digital Micrograph software.[45,46] The positions of atom columns in HAADF-STEM images were determined based on the two-dimensional Gaussian fitting, which was carried out by using the Matlab software.[47]

PFM Measurements: The PFM measurements were conducted using a scanning probe microscope (Cypher, Asylum Research) at room temperature. The conductive silicon cantilever with a Pt/Ir coating (ARROW-EFM-50, NanoWorld) was employed for local PFM hysteresis loop measurements. This cantilever has a length of 240 µm, a width of 35 µm, a resonance frequency of 75 kHz, and a force constant of 2.8 N/m. Prior to the measurements, the cantilever was calibrated by using Sader and thermal noise methods,[48,49] which was carried out by Asylum software (Asylum Research).

Phase Field Simulations: The polarization distribution in PTO films was studied by phase field simulations. The order parameters were chosen as the three components of spontaneous polarizations. The system's free energy was composed of bulk, gradient, elastic and electrostatic ones:

$$F = \int_V \left[f_{bulk}(P_i) + f_{grad}(P_{i,j}) + f_{elas}(P_i, \varepsilon_{kl}) + f_{elec}(P_i, E_i) \right] dV \tag{1}$$

The first term was the bulk energy density:

$$\begin{aligned} f_{bulk} = {} & \alpha_1 \left(P_1^2 + P_2^2 + P_3^2\right) + \alpha_{11} \left(P_1^4 + P_2^4 + P_3^4\right) \\ & + \alpha_{12} \left(P_1^2 P_2^2 + P_2^2 P_3^2 + P_1^2 P_3^2\right) + \alpha_{111} \left(P_1^6 + P_2^6 + P_3^6\right) \\ & + \alpha_{112} \left[P_1^4 \left(P_2^2 + P_3^2\right) + P_2^4 \left(P_1^2 + P_3^2\right) + P_3^4 \left(P_1^2 + P_2^2\right)\right] \\ & + \alpha_{123} P_1^2 P_2^2 P_3^2 \end{aligned} \tag{2}$$

The second term was the gradient energy density:

$$\begin{aligned} f_{grad} = {} & \frac{1}{2} G_{11} \left(P_{1,1}^2 + P_{2,2}^2 + P_{3,3}^2\right) + G_{12} \left(P_{1,1} P_{2,2} + P_{2,2} P_{3,3} + P_{1,1} P_{3,3}\right) \\ & + \frac{1}{2} G_{44} \left[\left(P_{1,2} + P_{2,1}\right)^2 + \left(P_{2,3} + P_{3,2}\right)^2 + \left(P_{3,1} + P_{1,3}\right)^2\right] \end{aligned} \tag{3}$$

The third term was the elastic energy density:

$$f_{elas} = \frac{1}{2} C_{ijkl} \left(\varepsilon_{ij} - \varepsilon_{ij}^0\right) \left(\varepsilon_{kl} - \varepsilon_{kl}^0\right) \tag{4}$$

where ε_{ij} was the total strain and ε_{ij}^0 was the spontaneous strain. Their difference was the elastic strain. The spontaneous strain $\varepsilon_{ij}^0 = Q_{ijkl} P_k P_l$ was related to the polarization by the electrostrictive coefficients Q_{ijkl}. The last term was the electrostatic energy density:

$$f_{elec} = -\frac{1}{2} \varepsilon_0 \varepsilon_b E_i^2 - E_i P_i \tag{5}$$

where ε_0 was the permittivity of vacuum and ε_b was the background relative dielectric constant.

It was assume that the equilibrium of mechanical stress and electrical field was much faster than the evolution of domain structures. Thus, the mechanical equilibrium equation $\sigma_{ij,j} = 0$ and the Maxwell equation $D_{i,i} = 0$ were solved to obtain the corresponding driving forces for each polarization configuration.

The evolution of polarization was governed by the time-dependent Ginzburg-Landau equation:

$$\frac{dP_i}{dt} = -L \frac{\delta F}{\delta P_i} \tag{6}$$

where L was the dynamic coefficient. The backward Euler method was used to trace the evolution of polarizations.

The sizes of the first and third models were $128 \times 128 \times 100$, corresponding to the real space size of $128 \times 128 \times 20$ nm^3, which contains the down layer (5 nm), the PTO film (5 nm) and the top layer (10 nm). The size of the second model was $128 \times 128 \times 10$ nm^3, i.e., no top layer. The surface of the top layer was in a traction-free state, while the bottom of the down layer was fixed to the substrate strain. All coefficients of PTO were adopted from previous literature.[50] For the sake of simplicity, the elastic constants of the whole system were chosen as the same as those of PTO.

Supporting Information

Supporting Information is available from the Wiley Online Library or from the author.

Acknowledgements

This work was supported by the Guangdong Basic and Applied Basic Research Foundation (No. 2023A1515011058), Guangdong Provincial Quantum Science Strategic Initiative (No. GDZX2302001, GDZX2402001) and the National Natural Science Foundation of China (Nos. 52122101, 52471022, and U24A2013). Y.J.W. acknowledges the Youth Innovation Promotion Association CAS (2021187), the Liaoning Revitalization Talents Program (XLYC2203020) and the open research fund of Songshan Lake Materials Laboratory (2023SLABFK13). Y.L.T. acknowledges the IMR Innovation Fund (2024-ZD01).

Conflict of Interest

The authors declare no conflict of interest.

Data Availability Statement

The data that support the findings of this study are available from the corresponding author upon reasonable request.

Keywords

ferroelectric thin films, interfacial engineering, topological domains, transmission electron microscopy

Received: April 25, 2025
Revised: June 15, 2025

[1] Y. L. Tang, Y. L. Zhu, X. L. Ma, A. Y. Borisevich, A. N. Morozovska, E. A. Eliseev, W. Y. Wang, Y. J. Wang, Y. B. Xu, Z. D. Zhang, S. J. Pennycook, *Science* **2015**, *348*, 547.

[2] A. K. Yadav, C. T. Nelson, S. L. Hsu, Z. Hong, J. D. Clarkson, C. M. Schlepütz, A. R. Damodaran, P. Shafer, E. Arenholz, L. R. Dedon, D. Chen, A. Vishwanath, A. M. Minor, L. Q. Chen, J. F. Scott, L. W. Martin, R. Ramesh, *Nature* **2016**, *530*, 198.

[3] S. Das, Y. L. Tang, Z. Hong, M. A. P. Gonçalves, M. R. McCarter, C. Klewe, K. X. Nguyen, F. Gómez-Ortiz, P. Shafer, E. Arenholz, V. A. Stoica, S.-L. Hsu, B. Wang, C. Ophus, J. F. Liu, C. T. Nelson, S. Saremi, B. Prasad, A. B. Mei, D. G. Schlom, J. Íñiguez, P. García-Fernández, D. A. Muller, L. Q. Chen, J. Junquera, L. W. Martin, R. Ramesh, *Nature* **2019**, *568*, 368.

[4] Y. J. Wang, Y. P. Feng, Y. L. Zhu, Y. L. Tang, L. X. Yang, M. J. Zou, W. R. Geng, M. J. Han, X. W. Guo, B. Wu, X. L. Ma, *Nat. Mater.* **2020**, *19*, 881.

[5] Y.-J. Wang, Y.-P. Feng, Y.-L. Tang, Y.-L. Zhu, Y. i. Cao, M.-J. Zou, W.-R. Geng, X.-L. Ma, *Nat. Commun.* **2024**, *15*, 3949.

[6] F.-H. Gong, Y.-L. Tang, Y.-L. Zhu, H. Zhang, Y. u.-J. Wang, Y. u.-T. Chen, Y.-P. Feng, M.-J. Zou, B. o. Wu, W.-R. Geng, Y. Cao, X.-L. Ma, *Sci. Adv.* **2021**, *7*, abg5503.

[7] W. R. Geng, Y. L. Zhu, M. X. Zhu, Y. L. Tang, H. J. Zhao, C. H. Lei, Y. J. Wang, J. H. Wang, R. J. Jiang, S. Z. Liu, X. Y. San, Y. P. Feng, M. J. Zou, X. L. Ma, *Nat. Nanotechnol.* **2025**, *20*, 366.

[8] C. Tan, Y. Dong, Y. Sun, C. Liu, P. Chen, X. Zhong, R. Zhu, M. Liu, J. Zhang, J. Wang, K. Liu, X. Bai, D. Yu, X. Ouyang, J. Wang, P. Gao, Z. Luo, J. Li, *Nat. Commun.* **2021**, *12*, 4620.

[9] A. Y. Abid, Y. Sun, X. Hou, C. Tan, X. Zhong, R. Zhu, H. Chen, K. e. Qu, Y. Li, M. Wu, J. Zhang, J. Wang, K. Liu, X. Bai, D. Yu, X. Ouyang, J. Wang, J. Li, P. Gao, *Nat. Commun.* **2021**, *12*, 2054.

[10] Q. Zhang, L. Xie, G. Liu, S. Prokhorenko, Y. Nahas, X. Pan, L. Bellaiche, A. Gruverman, N. Valanoor, *Adv. Mater.* **2017**, *29*, 1702375.

[11] I. I. Naumov, L. Bellaiche, H. Fu, *Nature* **2004**, *432*, 737.

[12] J. Ma, J. Ma, Q. Zhang, R. Peng, J. Wang, C. Liu, M. Wang, N. Li, M. Chen, X. Cheng, P. Gao, L. Gu, L.-Q. Chen, P. Yu, J. Zhang, C. E.-W. Nan, *Nat. Nanotechnol.* **2018**, *13*, 947.

[13] W. Yang, G. Tian, Y. Zhang, F. Xue, D. Zheng, L. Zhang, Y. Wang, C. Chen, Z. Fan, Z. Hou, D. Chen, J. Gao, M. Zeng, M. Qin, L.-Q. Chen, X. Gao, J.-M. Liu, *Nat. Commun.* **2021**, *12*, 1306.

[14] A. K. Yadav, K. X. Nguyen, Z. Hong, P. García-Fernández, P. Aguado-Puente, C. T. Nelson, S. Das, B. Prasad, D. Kwon, S. Cheema, A. I. Khan, C. Hu, J. Íñiguez, J. Junquera, L.-Q. Chen, D. A. Muller, R. Ramesh, S. Salahuddin, *Nature* **2019**, *565*, 468.

[15] Q. Li, V. A. Stoica, M. Pasciak, Y. i. Zhu, Y. Yuan, T. Yang, M. R. McCarter, S. Das, A. K. Yadav, S. Park, C. Dai, H. J. Lee, Y. Ahn, S. D. Marks, S. Yu, C. Kadlec, T. Sato, M. C. Hoffmann, M. Chollet, M. E. Kozina, S. Nelson, D. Zhu, D. A. Walko, A. M. Lindenberg, P. G. Evans, L.-Q. Chen, R. Ramesh, L. W. Martin, V. Gopalan, J. W. Freeland, et al., *Nature* **2021**, *592*, 376.

[16] R. Ramesh, D. G. Schlom, *Nat. Rev. Mater.* **2019**, *4*, 257.

[17] S. Chen, S. Yuan, Z. Hou, Y. Tang, J. Zhang, T. Wang, K. Li, W. Zhao, X. Liu, L. Chen, L. W. Martin, Z. Chen, *Adv. Mater.* **2020**, *33*, 2000857.

[18] Y. L. Tang, Y. L. Zhu, X. L. Ma, *J. Appl. Phys.* **2021**, *129*, 200904.

[19] X. Li, C. Tan, C. Liu, P. Gao, Y. Sun, P. Chen, M. Li, L. Liao, R. Zhu, J. Wang, Y. Zhao, L. Wang, Z. Xu, K. Liu, X. Zhong, J. Wang, X. Bai, *Proc. Natl. Acad. Sci. USA* **2020**, *117*, 18954.

[20] R. Zhu, Z. Jiang, X. Zhang, X. Zhong, C. Tan, M. Liu, Y. Sun, X. Li, R. Qi, K. e. Qu, Z. Liu, M. Wu, M. Li, B. Huang, Z. Xu, J. Wang, K. Liu, P. Gao, J. Wang, J. Li, X. Bai, *Phys. Rev. Lett.* **2022**, *129*, 107601.

[21] Y. u.-T. Shao, S. Das, Z. Hong, R. Xu, S. Chandrika, F. Gómez-Ortiz, P. García-Fernández, L.-Q. Chen, H. Y. Hwang, J. Junquera, L. W. Martin, R. Ramesh, D. A. Muller, *Nat. Commun.* **2023**, *14*, 1355.

[22] P. Tong, L. Zhou, K. Du, M. Zhang, Y. Sun, T. Sun, Y. Wu, Y. Liu, H. Guo, Z. Hong, Y. Xie, H. e. Tian, Z. e. Zhang, *Nat. Phys.* **2025**, *21*, 464.

[23] L. Zhou, Y. Huang, S. Das, Y. Tang, C. Li, H. e. Tian, L.-Q. Chen, Y. Wu, R. Ramesh, Z. Hong, *Matter* **2022**, *5*, 1031.

[24] Y. Liu, Y.-L. Zhu, Y.-L. Tang, Y. u.-J. Wang, Y. i.-X. Jiang, Y.-B. Xu, B. Zhang, X.-L. Ma, *Nano Lett.* **2017**, *17*, 3619.

[25] C. Lichtensteiger, J. M. Triscone, J. Junquera, P. Ghosez, *Phys. Rev. Lett.* **2005**, *94*, 047603.

[26] H.-H. Huang, Z. Hong, H. L. Xin, D. Su, L.-Q. Chen, G. Huang, P. R. Munroe, N. Valanoor, *ACS Nano* **2016**, *10*, 10126.

[27] S. Li, Y. L. Zhu, Y. J. Wang, Y. L. Tang, Y. Liu, S. R. Zhang, J. Y. Ma, X. L. Ma, *Appl. Phys. Lett.* **2017**, *111*, 052901.

[28] M. Hadjimichael, Y. Li, E. Zatterin, G. A. Chahine, M. Conroy, K. Moore, E. N. O.' Connell, P. Ondrejkovic, P. Marton, J. Hlinka, U. Bangert, S. Leake, P. Zubko, *Nat. Mater.* **2021**, *20*, 495.

[29] J. J. P. Peters, G. Apachitei, R. Beanland, M. Alexe, A. M. Sanchez, *Nat. Commun.* **2016**, *7*, 13484

[30] L. Pintilie, I. Vrejoiu, D. Hesse, M. Alexe, *J. Appl. Phys.* **2008**, *104*, 114101.

[31] S. R. Spurgeon, J. D. Sloppy, D. M. (.D.). Kepaptsoglou, P. V. Balachandran, S. Nejati, J. Karthik, A. R. Damodaran, C. L. Johnson, H. Ambaye, R. Goyette, V. Lauter, Q. M. Ramasse, J. C. Idrobo, K. K. S. Lau, S. E. Lofland, J. M. Rondinelli, L. W. Martin, M. L. Taheri, *ACS Nano* **2014**, *8*, 894.

[32] R. Jacobs, J. Booske, D. Morgan, *Adv. Funct. Mater.* **2016**, *26*, 5471.

[33] Y. P. Feng, H. Wu, Y. L. Zhu, Y. J. Wang, Y. L. Tang, X. L. Ma, *Adv. Mater.* **2025**, *37*, 2414346.

[34] Z. Hong, A. R. Damodaran, F. Xue, S.-L. Hsu, J. Britson, A. K. Yadav, C. T. Nelson, J.-J. Wang, J. F. Scott, L. W. Martin, R. Ramesh, L.-Q. Chen, *Nano Lett.* **2017**, *17*, 2246.

[35] Z. Hong, L.-Q. Chen, *Acta Mater.* **2018**, *15*, 155
[36] S. Li, Y. J. Wang, Y. L. Zhu, Y. L. Tang, Y. Liu, J. Y. Ma, M. J. Han, B. Wu, X. L. Ma, *Acta Mater.* **2019**, *171*, 176
[37] Z. Li, Y. Wang, G. Tian, P. Li, L. Zhao, F. Zhang, J. Yao, H. Fan, X. Song, D. Chen, Z. Fan, M. Qin, M. Zeng, Z. Zhang, X. Lu, S. Hu, C. Lei, Q. Zhu, J. Li, X. Gao, J.-M. Liu, *Sci. Adv.* **2017**, *3*, 1700919.
[38] M.-J. Han, Y.-J. Wang, Y.-L. Tang, Y.-L. Zhu, J.-Y. Ma, W.-R. Geng, M.-J. Zou, Y.-P. Feng, N.-B. Zhang, X.-L. Ma, *J. Phys. Chem. C* **2019**, *123*, 2557.
[39] A. Chaudron, Z. Li, A. Finco, P. Marton, P. Dufour, A. Abdelsamie, J. Fischer, S. Collin, B. Dkhil, J. Hlinka, V. Jacques, J.-Y. Chauleau, M. Viret, K. Bouzehouane, S. Fusil, V. Garcia, *Nat. Mater.* **2024**, *23*, 905.
[40] B. J. Rodriguez, C. Callahan, S. V. Kalinin, R. Proksch, *Nanotechnology* **2007**, *18*, 475504.
[41] J. J. Peng, C. Song, B. Cui, F. Li, H. J. Mao, G. Y. Wang, F. Pan, *Appl. Phys. Lett.* **2015**, *107*, 182904.
[42] R. Xu, S. Liu, I. Grinberg, J. Karthik, A. R. Damodaran, A. M. Rappe, L. W. Martin, *Nat. Mater.* **2015**, *14*, 79.
[43] R. J. Xu, J. Karthik, A. R. Damodaran, L. W. Martin, *Nat. Commun.* **2014**, *5*, 3120
[44] W. Weng, C. Ortolland, presented at European Microscopy Congress Proceedings, Wiley, New York, Chichester, UK **2016**.
[45] M. J. Hytch, E. Snoeck, R. Kilaas, *Ultramicroscopy* **1998**, *74*, 131.
[46] Y. L. Tang, Y. L. Zhu, X. L. Ma, *Ultramicroscopy* **2016**, *160*, 57
[47] S. M. Anthony, S. Granick, *Langmuir* **2009**, *25*, 8152.
[48] J. L. Hutter, J. Bechhoefer, *Rev. Sci. Instrum.* **1993**, *64*, 1868.
[49] J. E. Sader, J. W. M. Chon, P. Mulvaney, *Rev. Sci. Instrum.* **1999**, *70*, 3967.
[50] Y. L. Li, S. Y. Hu, Z. K. Liu, L. Q. Chen, *Acta Mater.* **2002**, *50*, 395.

RESEARCH ARTICLE

ADVANCED MATERIALS
www.advmat.de

Observation of Néel-Skyrmions in Bilayered Oxide Ferroelectrics

Feng-Hui Gong, Shuai-Shuai Yin, Kefan Liu, Yun-Long Tang, Yin-Lian Zhu, Yu-Ting Chen, Yu-Jia Wang, Xiao-Long Li, Xue-Rong Liu, Zijian Hong, and Xiu-Liang Ma**

Skyrmions in ferromagnetic materials exhibit either Néel or Bloch characteristics. Although skyrmions in ferromagnetic materials can be readily obtained via inter-spin interactions, a skyrmion in ferroelectric materials exhibiting solely Néel or Bloch characteristics has not yet been discovered. Here, by modulating the formation of skyrmion-bubbles in [(PbTiO$_3$)$_n$/(SrTiO$_3$)$_n$]$_1$ [(PTO$_n$/STO$_n$)$_1$] bilayers grown on STO substrates, the atomic morphology of pure Néel-skyrmion is observed with a topological charge of ± 1 in the ultrathin bilayered films with the thickness of 2 unit cells (u.c.). Such a pure Néel-skyrmion is confirmed by a combination of atomic mappings, geometric phase analysis, and X-ray 3D reciprocal space mapping (RSM). It is found that decreasing the thickness of bilayered films from 50 to 2 u.c., the characteristics of skyrmion-bubbles exhibiting both Néel and Bloch features disappear along with the Bloch features. The formation mechanism of the Néel-skyrmions is unveiled using Phase-field simulations, showing the critical role of electric and gradient energy variation in the stable phase of Néel-skyrmions. These nanoscale pure Néel-skyrmions represent the electrical equivalents of their magnetic counterparts, extending the size limits of topological phases and offering potential advancements in the field of ferroelectric physics.

1. Introduction

Topological structures based on spin and polarization share many similarities, such as flux closures,[1–6] vortices,[7–20] center-type domains,[21–23] and labyrinthine.[24] However, there are significant structural differences between the skyrmion-bubbles[25–39] (also known as polar skyrmions) in ferroelectric materials and the skyrmion in magnetic materials (Figure S1, Supporting Information). Skyrmions in magnetic materials exhibit either Néel or Bloch characteristics, whereas skyrmion bubbles in ferroelectric materials exhibit mixed characteristics. The Néel and Bloch components of polarization rotations describe these complex dipole patterns.[39] In Néel domain walls, the rotation of polarizations occurs in the plane perpendicular to the domain wall, producing a non-zero projection of the order parameter on the domain wall's normal.

F.-H. Gong, Y.-L. Zhu, Y.-T. Chen, X.-L. Ma
Bay Area Center for Electron Microscopy
Songshan Lake Materials Laboratory
Dongguan, Guangdong 523808, China
E-mail: xlma@iphy.ac.cn

F.-H. Gong, Y.-T. Chen, X.-L. Ma
Institute of Physics
Chinese Academy of Sciences
Beijing 100190, China

S.-S. Yin, X.-R. Liu
School of Physical Science and Technology
ShanghaiTech University
Shanghai 201210, China

K. Liu, Z. Hong
State Key Laboratory of Silicon and Advanced Semiconductor Materials
School of Materials Science and Engineering
Zhejiang University
Hangzhou, Zhejiang 310058, China
E-mail: hongzijian100@zju.edu.cn

The ORCID identification number(s) for the author(s) of this article can be found under https://doi.org/10.1002/adma.202501411

DOI: 10.1002/adma.202501411

Y.-L. Tang, Y.-J. Wang
Shenyang National Laboratory for Materials Science
Institute of Metal Research
Chinese Academy of Sciences
Shenyang 110016, China

Y.-L. Tang, Y.-J. Wang
School of Materials Science and Engineering
University of Science and Technology of China
Shenyang 110016, China

Y.-L. Zhu
School of Materials Science and Engineering
Hunan University of Science and Technology
Xiangtan 411201, China

X.-L. Li
Shanghai Synchrotron Radiation Facility (SSRF)
Shanghai Advanced Research Institute
Chinese Academy of Sciences
Shanghai 200120, China

X.-R. Liu
Center for Transformative Science
ShanghaiTech University
Shanghai 201210, China

Z. Hong
Institute of Fundamental and Transdisciplinary Research
Zhejiang University
Hangzhou 310058, China

In contrast, polarization rotation across Bloch domain walls occurs in the domain wall's plane.[39] Therefore, the search for pure Néel-type or Bloch-type ferroelectric skyrmions could enhance the analogy between ferroelectric and ferromagnetic materials, potentially advancing the research of ferroelectric physics and driving the design of ultrathin electronic devices.

Over the past five years, systematic explorations of ferroelectric skyrmion-bubbles from both experimental and theoretical perspectives[25–39] have revealed their stabilization by the complex interplay among bulk, gradient, elastic, and electrostatic energies. These skyrmion-bubbles exhibit exotic properties such as chirality,[26,40] negative capacitance,[28,41–43] and topological phase transition behavior.[30,32,33,35] However, as a difference to the Dzyaloshinskii-Moriya interaction, dipole–dipole interactions are achiral, meaning that they energetically favor Bloch-skyrmions.[44–46] The formation of ferroelectric Néel-skyrmions necessitates a significant electric charge to compensate for the divergence of the radial gradients in electric polarization.[25,47,48] Similarly, domain engineering is a feasible strategy for creating diverse, weakly correlated Néel-skyrmions and Bloch-skyrmions in single-layer tetragonal ferroelectric thin films.[49] Therefore, previous theoretical studies have suggested that the existence of Néel-skyrmions is relatively unlikely, making their detection and study more challenging.

Experimentally, previous studies have focused on the $[(\mathrm{PbTiO_3})_n/(\mathrm{SrTiO_3})_n]_m$ $(\mathrm{PTO}_n/\mathrm{STO}_n)_m$ superlattice system. Significant fluctuations in the skyrmion-bubble domain morphology have been observed in $(\mathrm{PTO}_{16}/\mathrm{STO}_{16})_1$ bilayer films.[26] Inspired by the bilayer system, reducing the bilayer film thickness to a few u.c. may reveal novel structures primarily governed by gradient energy. Therefore, in this work, we aim to identify pure Néel ferroelectric skyrmions and elucidate the evolutionary behavior of skyrmion-bubbles with varying thicknesses by growing a series of $(\mathrm{PTO})_n/(\mathrm{STO})_n$ bilayers on STO substrates using pulsed laser deposition (PLD).

2. Results and Discussion

PTO is a tetragonal structure at room temperature with the lattice parameters of $a = b = 3.899$ Å and $c = 4.153$ Å. **Figure 1a** illustrates the crystal structure of PTO. The ferroelectricity in PTO can be explained at four levels: i) Displacement ferroelectrics involve significant displacements of Pb^{2+} and Ti^{4+} cations relative to O^{2-} anions within the tetragonal u.c., leading to a separation of the positive and negative charge centers, forming an electric dipole or spontaneous polarization ($\boldsymbol{P}_s$), as shown in Figure 1b. The δ_{Ti} vector in each u.c. opposes the polarization direction of PTO. The integrated differential phase contrast (iDPC) imaging method enhances imaging contrast for light elements and reduces the impact of multiple scattering on images. However, iDPC requires algorithms for image reconstruction and demands computational resources. The annular bright-field (ABF) imaging method also improves imaging contrast for light elements, with relatively simple image processing. It does not require iterative algorithms for real-time imaging. The image quality of ABF relies on the angular resolution of the transmission electron beam. In the iDPC image of a partial ferroelectric skyrmion-bubble (Figure 1c), the atomic shift between cations and anions is visible, with the shift between cations and O atoms being more pronounced than that between Pb and Ti. ii) From a classical mechanics perspective, the paraelectric-ferroelectric phase transition in PTO results in a polar lattice, driven by the competition between short-range repulsions and long-range Coulomb forces. iii) In terms of electronic structure, the PTO's ferroelectricity originates from the synergistic interaction between the lone pair electrons of Pb and the d_0 mechanism. The 6d orbital of Pb is not fully occupied, the oxygen octahedral undergoes Jahn-Teller distortion, leading to crystal field splitting. This alters the electron cloud of Ti, resulting in polarity within the PTO u.c. iv) Lattice dynamics reveal that ferroelectricity is induced by phonon splitting and the softening of the optical branch transverse mode in the central Brillouin zone.

Figure 1d–g shows the cross-sectional high-angle annular dark-field scanning transmission electron microscopy (HAADF-STEM) images of $(\mathrm{PTO}_n/\mathrm{STO}_n)_1$ bilayers with varying thicknesses grown on STO substrates. The substrate/PTO and PTO/STO interfaces appear flat (indicated by two pairs of white arrows in Figure 1d–g). Atomic-resolved X-ray energy dispersive spectroscopy (EDS) was acquired to identify the element distribution in the film, as shown in Figure S2 (Supporting Information). It is seen that both interfaces are very sharp, and there is no indication of inter-diffusion. Additionally, the single-crystal structure of the samples was characterized at the BL02U2 Station of Shanghai Synchrotron Radiation Facility (SSRF), with a spot size of ≈160 × 80 um after focusing, and statistically evaluated the structure of the single-crystal samples at a large scale (hundred-micron scale). Crystal truncation rod (CTR) 00L data of $(\mathrm{PTO_2}/\mathrm{STO_2})_1$ samples were acquired, and the structure of epitaxial thin films was reconstructed by the COBRA algorithm (Figure 1h).[50–52] The electron density (ED) distribution of the epitaxial film was obtained (Figure 1i), and we can visualize the obvious density difference between the substrate and the epitaxial film from the ED distribution envelope. And the atomic layer of the epitaxial film is clear, indicating high sample quality. Based on the Gaussian fit from Figure 1i, we can determine that the terminal layer of the STO substrate is $\mathrm{TiO_2}$, and 2/2 u.c. PTO/STO films were grown on STO substrates. The occupancy rate of the uppermost layer of Pb is slightly lower, likely due to certain mixing of Pb and Sr (Figure 1j,k). The outermost layer was flat-layered with a 2 u.c. STO film, and the sample surface was a $\mathrm{TiO_2}$ terminal surface. The increase in the HWHM of STO on the surface indicates that the 2 u.c. STO layer is polarized, possibly due to the influence of the PTO polarization (Figure 1k). These results suggest that we have obtained high-quality PTO/STO bilayers, which is important for further revealing the characteristics of possible polar topologies.

X.-L. Ma
Quantum Science Center of Guangdong-HongKong-Macau Greater Bay Area
Shenzhen, China
X.-L. Ma
State Key Lab of Advanced Processing and Recycling on Non-ferrous Metals
Lanzhou University of Technology
Lanzhou 730050, China

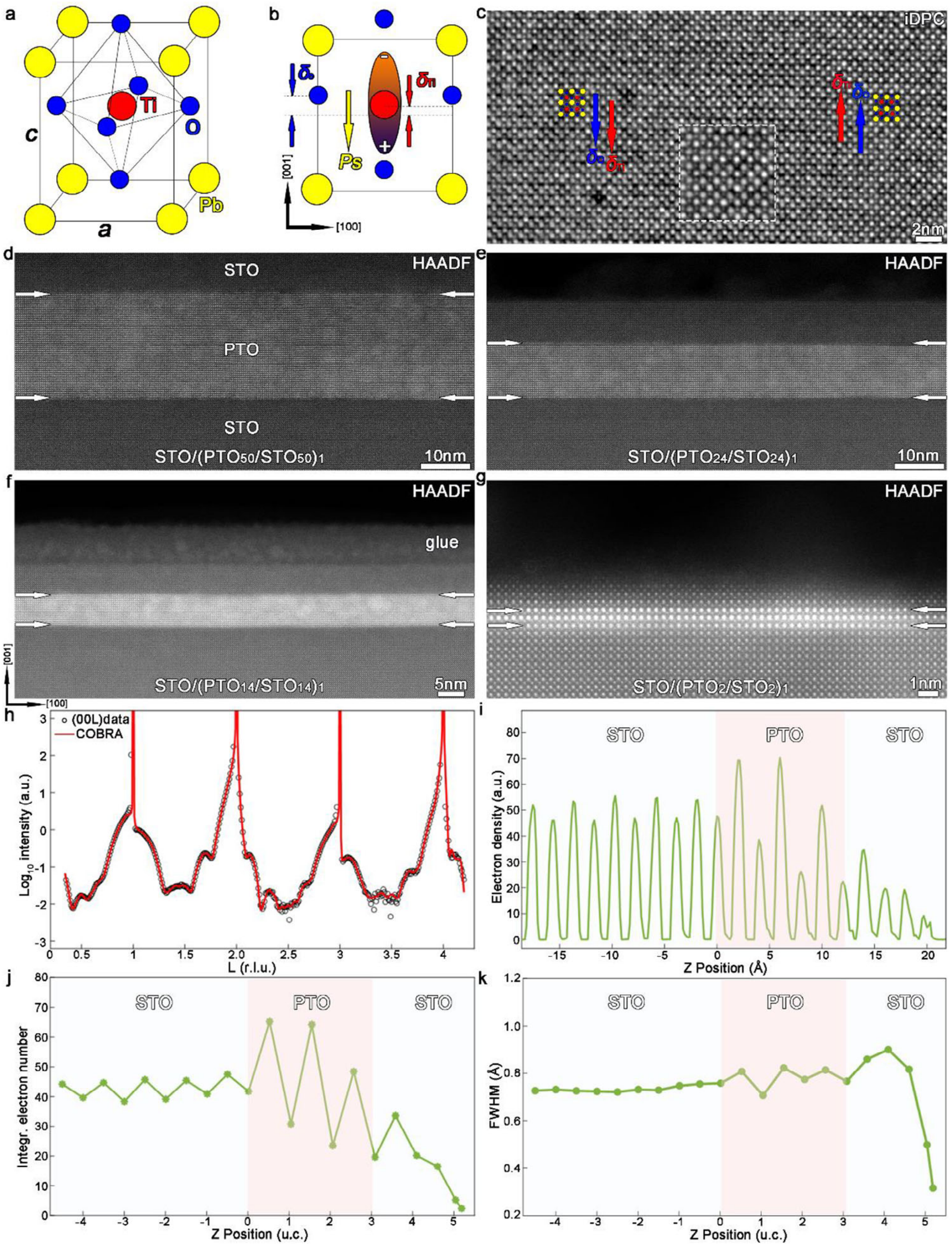

Figure 1. Characterization of the growth quality of PTO/STO bilayers. a) Schematic perspective view of the u.c. of $PbTiO_3$ (yellow, Pb; red, Ti; blue, O). b) Projection of the u.c. along the [010] direction. c) iDPC image of the $PbTiO_3$ crystal along the [010] direction. d–g) Cross-sectional high-resolution HAADF-STEM image for $(PTO_n/STO_n)_1$ (n = 50, 24, 14, 2 u.c.) bilayers. h) CTR 00L data (solid black circle) and COBRA calculation data (red line). i) Z-direction electron density distribution of the epitaxial film obtained by using the COBRA phase reconstruction algorithm. j) Integral area distribution obtained by Gaussian fitting based on the electron density distribution of (i). k) Full width at half maximum (FWHM) obtained by Gaussian fitting based on the electron density distribution of (i).

We have further applied iDPC imaging, which is more sensitive for recording O atom columns (Figure S3a, Supporting Information). And we have precisely measured ion displacement and polarization near the domain wall of the skyrmion-bubble. The reversed δ_{Ti} and δ_{O} vector maps reveal domain wall curved characteristics of skyrmion-bubble (FigureS3b,c, Supporting Information). The results of determining the polarization direction based on the displacement of Ti^{4+} and O^{2-} are consistent. Additionally, we separately extracted the displacements of O1, O2, and Ti along the out-of-plane direction (Figure S3d–f, Supporting Information). O1 represents the oxygen within the in-plane of the oxygen octahedron, while O2 represents the oxygen at the upper and lower vertices of the oxygen octahedron. The out-of-plane displacement of O1 ranges from −60 to 85 pm, moving from the left side to the right side of the domain wall (Figure S3d, Supporting Information), while the out-of-plane displacement of

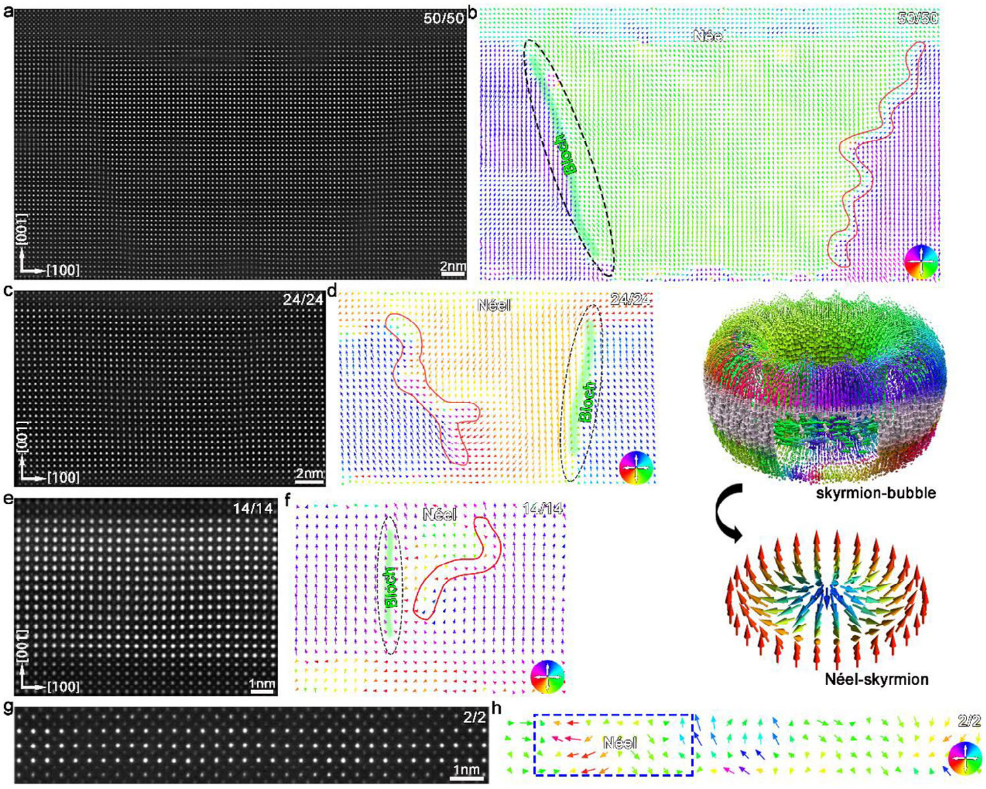

Figure 2. Thickness-dependent skyrmions phase transition. a-h) A series of cross-sectional HAADF-STEM images for $(PTO_n/STO_n)_1$ ($n = 50, 24, 14, 2$ u.c.) bilayers and their corresponding polarization maps. The right illustration is the 3D skyrmion transformation maps.[34]

O2 is −50 to 55 pm (Figure S3e, Supporting Information). Interestingly, the displacement of O1 is greater than that of O2. The out-of-plane displacement of Ti^{4+} is −29 to 43 pm from the left side of the domain wall to the right (Figure S3f, Supporting Information). By comparison, the displacement of O2 is greater than that of Ti^{4+}. In addition, we also extracted the tetragonality for the 10th, 11th, 21st, and 22nd PTO u.c. layers, as marked by white arrows (Figure S3a,g, Supporting Information). The tetragonality in Bloch regions (domain wall) is smaller than the tetragonality in other regions (Figure S3g, Supporting Information). To get further insight into the polarization distributions, we calculated the out-of-plane component of polarization ($|P_s|_z$) based on the empirical formula:[53]

$$Ps = k\delta Ti \tag{1}$$

and calculated the out-of-plane and in-plane component of polarization ($|P_s|_z$ and $|P_s|_x$) based on formula:[54]

$$Ps = \frac{e}{V}\sum_{i=1}^{N} Zi \ \ast\delta Ti \tag{2}$$

where P_s (μC cm^{-2}) is the calculated $\boldsymbol{P}_s$ value of ferroelectric. For ferroelectric PTO, the value of k is ≈2726 (μC cm^{-2})/nm, δ_{Ti} (nm) is the displacement value of Ti^{4+} along the out-of-plane or in-plane direction, V is the volume of u.c. ($V = a^2c$), and the Born effective charge Z of atom i, calculated by ab initio theory, has numerical values of 6.71 for Ti, −2.56 for O1 and −5.51 for O2 (out-of-plane), and −2.56 for O1 and −2.56 for O2 (in-plane). The polarization value in the out-of-plane direction gradually decreases and then increases, while the polarization value in the in-plane direction gradually increases and then decreases (Figure S3h–j, Supporting Information).

Next, to explore the evolutionary behavior of skyrmion-bubbles with varying film thickness, we acquired atomically resolved HAADF-STEM images for $(PTO_n/STO_n)_1$ ($n = 50, 24, 14, 2$ u.c.) bilayers, along with corresponding polarization maps (**Figure 2**; Figure S4, Supporting Information). In HAADF-STEM images, the Pb^{2+} columns appear as the brightest dots because the intensity of atom columns is approximately proportional to Z^2, where Z is the atomic number. The Ti^{4+} columns show weaker contrast. Note that enhanced darker and brighter contrast exists in 50 and 24 u.c. thick PTO layers, suggesting that twisted skyrmion-bubble domain walls emerge in PTO layers (Figure 2a,c). When the PTO thickness is reduced to ≈14 u.c., the distinct domain wall contrast disappears, and we have to roughly determine the position of the domain wall by ionic displacement during the experiment (Figure 2e,g). The polarization maps show that one side of the skyrmion-bubble domain wall exhibits severely twisted state (as marked by the red solid line) in the 50, 24, and 14 u.c. thick PTO layers (Figure 2b,d,f), while the other side of the domain wall appears relatively straight (as marked by black dotted line). In fact, previous work has indicated that the morphology of skyrmion-bubbles in bilayer films is more complex,[26] suggesting greater uncertainty in the evolution of domain configurations as the bilayer film thickness decreases. Interestingly, we found that the Néel and Bloch characteristics of the skyrmion-bubble are preserved in the 50, 24, and 14 u.c. thick PTO layers (Figure 2b,d,f).

In addition, the phase-field simulation confirmed the presence of Bloch-type skyrmion domain walls in thick films (Figure S5, Supporting Information). The cross-sectional polarization distribution shows that these tilted domain walls appear as closed-loop domains at the top and bottom of the PTO layer, with tilted torsion occurring in the middle (Figure S5a,b, Supporting Information). The in-plane polarization component at the center of the domain wall is relatively large, forming a Bloch-type domain wall, which is consistent with Figure S3 (Supporting Information). Furthermore, we calculated the helicity density distribution of the tilted domain walls (Figure S5c,d, Supporting Information). When the helicity is positive, it is defined as right-handed; otherwise, it is left-handed. Consequently, we identified two types of tilted domain walls: left-handed characteristic domain walls when tilted counterclockwise, and right-handed characteristic domain walls when rotated clockwise. Meanwhile, the skyrmion structure only exhibits the Néel feature in the 2 u.c. thick PTO layers (Figure 2g,h). For ferroelectric skyrmion-bubble and pure Néel-skyrmion, there is no obvious difference in the polarization distribution of the planar-view (Figure S6, Supporting Information).

We conducted geometric phase analysis (GPA) on PTO/STO bilayers of varying thicknesses, as illustrated in **Figure 3**a–h. ε_{xx} maps indicate that the STO_{sub}/PTO and PTO/STO_{film} interfaces are smooth and not sharp, as marked by white arrows, because the a of PTO ($a = 3.899$ Å) and STO ($a = 3.905$ Å) are very close. For ferroelectric skyrmion-bubble and Néel-skyrmion, there is no difference in the in-plane direction strain maps (Figure 3a–d). However, ε_{zz} maps indicate that these interfaces are sharp, as marked by white arrows, because the c of PTO ($c = 4.153$ Å) is much larger than that of STO ($c = 3.905$ Å). The PTO layers undergo tensile strain modulation in the out-of-plane direction, implying that the polarization direction is distributed along the out-of-plane direction (Figure 3e–g). In addition, we found enhanced and reduced strain features in the regions of skyrmion-bubble domain wall, which also reflects the bending characteristics of the domain wall in the $(PTO_n/STO_n)_1$ ($n = 50, 24, 14$ u.c.) bilayers (Figure 3e–g). So, the ε_{zz} strain maps (curved domain wall characteristics) also conform to the polarization mapping results in Figure 2b,d,f. When the PTO thickness was further reduced to 2 u.c., the upper STO layer exhibited localized tensile strain modulation, as marked by blue arrows, indicating that out-of-plane polarization has emerged. The middle PTO layer showed localized strain attenuation, as indicated by black arrows (Figure 3h). This abnormal strain state corresponds to the strain characteristics of a ferroelectric Néel-skyrmion.

The lattice Z (c value) extracted from atomic scale-resolved HAADF-STEM images (Figure 2a,c,e,g) is shown in Figure S7a–d (Supporting Information). The lattice Z changes sharply on the skyrmion-bubble curved domain wall (Figure S7a–c, Supporting Information). Figure 3i,j depicts the maximum, minimum, and average values of lattice Z and lattice X (a value). The average values of lattice Z and lattice X in different thick PTO/STO bilayers are consistent with the bulk value (pink dashed line). The shift Z (the Ti^{4+} displacement along the out-of-plane direction) extracted from atomic scale-resolved HAADF-STEM images (Figure 2a,c,e,g) is shown in Figure S7e–h (Supporting Information). Figure S3k,l (Supporting Information) depicts the maximum, minimum, and average values of shift Z and shift X (the Ti^{4+} displacement along the in-plane direction). As the film thickness decreases, the maximum and average values of shift Z gradually decrease. Because, in the cross-sectional view of the skyrmion-bubble, the polarization is predominantly along the out-of-plane direction across most regions, but at the core of the domain wall, polarization rotation causes the out-of-plane displacement to approach zero. As the thickness of the film decreases, the maximum value of shift X gradually decreases. However, when the PTO thickness reaches 2 u.c., the shift X suddenly increases, indicating the emergence of a significant in-plane displacement, which corresponds to the in-plane polarization characteristics of a ferroelectric Néel-skyrmion. The strain and ion displacement analysis also confirms the existence of pure Néel-skyrmion in 2/2 u.c. thick ultrathin bilayers. To ensure the reliability of the results, we can also select different crystallographic orientations for observation. This approach may minimize discrepancies between the fundamental features of the reconstructed 3D structure and its true characteristics. To further validate our experimental results, we also confirm them through other approaches, such as polarization maps, ion displacement, strain analysis, and synchrotron radiation.

To further confirm the significant structural changes observed in 2 u.c. thick PTO/STO bilayers, we utilized synchrotron-based XRD, as illustrated in Figure 3m–o. Based on the coordinates of diffraction spots in reciprocal space, we calculated the lattice constant corresponding to each diffraction spot. Then we found that the diffraction peaks of the STO film (labeled as 3, 5, 9, 11, 13) also appeared around the 011, 101, and 201 diffraction spots of the STO substrate, indicating that the lattice constant of the STO film does not match that of the STO substrate. Meanwhile, the separated diffraction peaks of the STO film also mean that the STO film comes into structural distortions, ion displacements, and polarity, which are consistent with analysis results of CTR data (Figure 1h–k) and polarization map (Figure 2g,h). The accumulation of charge on the sample surface and the penetration effect of PTO polarization have led to the polarity of the STO layer. In addition, we observed that the diffraction peaks of the PTO film (labeled as 2, 4, 6, 7, 8, 12, 14, 15, 16) appeared around the 011, 101, and 201 diffraction spots of the STO substrate. This suggests significant lattice constant fluctuations in the PTO film, implying a complex or rich polarization configuration. By comparing planar-view dark-field STEM images of $STO_{16}/PTO_{16}/STO_{16}$ trilayer and $(STO_{16}/PTO_{16})_8$ superlattice,[26] we find that the morphology of skyrmion-bubble in trilayers is severely bent and twisted. There are widespread occurrences of nanometre-size round and squiggly elongated features in trilayers. This also suggests that reducing the thickness of the trilayers to 2 u.c. may lead to significant structural changes in the skyrmion-bubble. The asymmetric multiple PTO diffraction peaks in the 011, 101, and 201 reciprocal space maps show that the topological domains have the characteristic of preferentially oriented arrangement (Figure 3m–o).

The polarization maps (Figure 2b,d,f) clearly illustrate the Bloch characteristics of the skyrmion-bubble, where the polarization forms closed loops, as indicated by the red solid line and black dashed line. It also reveals the Néel characteristics at the PTO/STO interface, where the polarization either converges or diverges. However, when the thickness of the PTO/STO film is reduced to 2 u.c., the Bloch polarization component with closed-loop characteristics disappears, leaving only the divergent

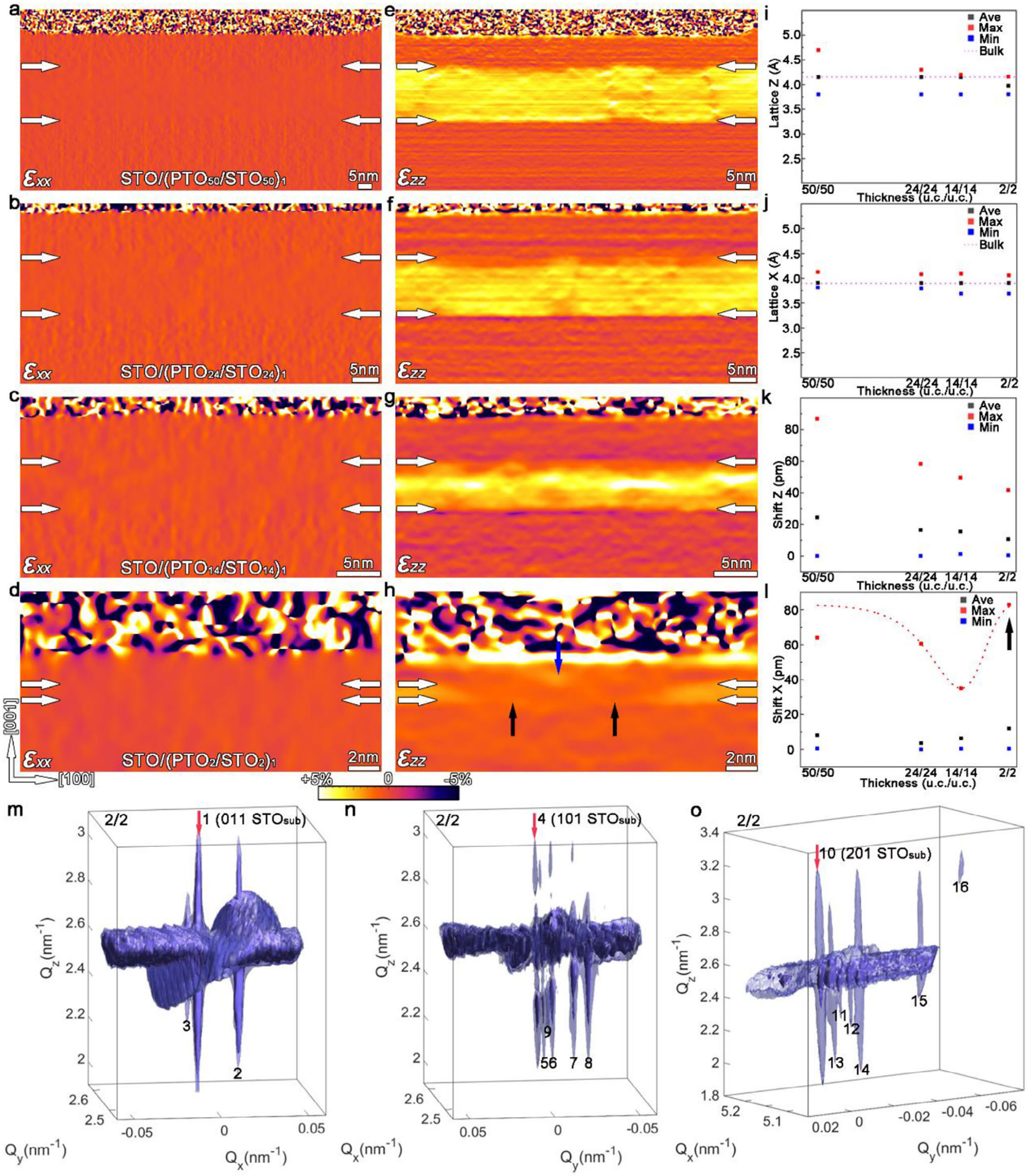

Figure 3. Strain, ion displacement, and 3D-RSM of ferroelectric Néel-skyrmion. a–d) The GPA analysis of in-plane strain ε_{xx}. e-h) The GPA analysis of out-of-plane normal strain ε_{zz}. White arrows indicate heterointerfaces in these photographs. i,j) Maximum, minimum, and average values of lattice Z (out-of-plane, *c* value) and lattice X (in-plane, $a = b$ value). k,l) Maximum, minimum, and average values of shift Z (δ_{Ti}) and shift X (δ_{Ti}). m-o) Local 3D RSM patterns of the (011), (101), and (201) for the $(\mathrm{PTO}_2/\mathrm{STO}_2)_1$ bilayers grown on STO substrates. (m) 1-STO$_{\mathrm{sub}}$, 2-PTO$_{\mathrm{film}}$, 3-STO$_{\mathrm{film}}$. (n) 4-STO$_{\mathrm{sub}}$, 5,9-STO$_{\mathrm{film}}$, 6,7,8-PTO$_{\mathrm{film}}$. (o) 10-STO$_{\mathrm{sub}}$, 11,13-STO$_{\mathrm{film}}$, 12,14,15,16-PTO$_{\mathrm{flim}}$.

polarization component; that is, only the Néel characteristics remain (Figure 2h). If Bloch characteristics were present, given that the PTO layer is only 2 u.c., closed polarization loops would appear in the in-plane field of view. But, in the in-plane field of view, the polarization distribution only shows convergence or divergence, corresponding to the pure Néel characteristics (Figure S6c, Supporting Information). Therefore, the polarization distributions in both the cross-sectional and in-plane fields of view confirm the existence of pure Néel-skyrmions in the PTO/STO bilayer film. The reproducible experimental evidence is presented in Figure S8 (Supporting Information). Next, the out-of-plane strain states at the core (marked by blue arrow) and edge regions of the Néel-skyrmion are consistent (Figure 3h). These regions experience out-of-plane tensile strain modulation, which corresponds to the positions of the blue and red polarization arrows in the schematic of the pure Néel-skyrmion (Figure 2). The maximum in-plane ion displacement (shift X) of the Néel-skyrmion is shown by the black arrows in Figure 3l, corresponding to the intermediate position where the polarization transitions from vertically upward to vertically downward (Figure 2, the schematic of the pure Néel-skyrmion). That is, it also corresponds to the position indicated by the black arrows in the out-of-plane strain map (Figure 3h). In addition, multiple parallel "subrod" signals near the Bragg peak are clearly observed in the 3D RSM patterns (Figure 3m–o), indicating the presence of domains with similar lattice constants in the film. This differs from the previously reported skyrmion-bubble signal. The experimental evidence collectively confirms the presence of pure Néel-skyrmions in the ultrathin bilayer film.

We also utilized phase-field simulations to unveil the origin of the polar Néel-skyrmions and to explain the evolution of skyrmion-bubble with varying thickness. The polar structure for $(\mathrm{PTO}_n/\mathrm{STO}_n)_{1n}$ bilayer films with different thicknesses is calculated (**Figure 4**). We present scattered point charges at the interface of the bilayer films to represent polarization charges. For thick $(\mathrm{PTO}_n/\mathrm{STO}_n)_1$ thin films ($n = 50, 24, 14$ u.c.), the in-plane polarization distribution indicates that skyrmion-bubbles mainly consist of bubbles and stripes (Figure 4a,b,c). As the film thickness decreases, the out-of-plane polarization intensity gradually diminishes due to the reduction of the $\boldsymbol{P}_s$. When the thickness decreased to 2 u.c., pure Néel-skyrmions appeared (Figure 4d,e). The cross-sectional views of the two types of skyrmions demonstrate the transition to Néel-skyrmions. From the center to the edge of the skyrmions, the out-of-plane component of the polarization vector first decreases and then increases, while the in-plane polarization component first increases and then decreases. At the center of the skyrmion wall, the in-plane polarization component reaches its maximum, and the out-of-plane polarization component reaches its minimum, forming a Néel-skyrmion. The topological charge of these Néel-skyrmions is calculated as ± 1. The number of skyrmions in the simulation box is counted (with a size of 78.4 nm × 78.4 nm, Figure 4f). The number of skyrmions increases significantly with the decrease in the PTO size, showing both the decreased skyrmion size and increased skyrmion density.

Moreover, to elucidate the reason for the emergence of Néel-skyrmions, the different energy components are calculated, e.g., the elastic, electric, Landau, and gradient energy densities (Figure 4g,h). As the thickness increases, the electric and gradient energy densities gradually increase, while the elastic and Landau energy densities decrease simultaneously. The total energy of the system decreases with increasing thickness due to the larger reduction in the Landau energy. We found that when the film decreases to 2 u.c., the total energy significantly increases by 3 orders of magnitude. Comparing each type of energy, it was found that the Landau energy density is the highest when $n = 2$. To minimize the total energy, the system chooses to stay in the tetragonal region that reduces the other polarization components, leading to the emergence of Néel-skyrmions. Here, we propose an explanation for the emergence of Néel-skyrmions from the perspective of the depolarization (which forms within the PTO layer sandwiched between the insulating STO layers) and the strain relaxation. The depolarization field strengths for the 2 and 16 u.c. PTO are 6.58 and 0.97 V nm^{-1} without the formation of skyrmions, respectively. In the superlattice with large periodicity (e.g., 16/16), the depolarization primarily affects only a few PTO u.c. near the STO/PTO interface, while some degrees of strain relaxation occur throughout the superlattice film, forming complex polar structures with both mixed characters. However, in our case with just 2 u.c. PTO, the depolarization field is stronger (favoring simple in-plane-polarization) while the strain relaxation is minimal (favoring simple out-of-plane polarization with large substrate strain), the combination of these two effects makes a much simpler physical picture of a pure Néel-skyrmion.

3. Conclusion

This work has demonstrated that the pure Néel polar skyrmions can be sustained in ultrathin bilayers, with the PTO layer being as thin as 2 u.c., as shown by both experimental observations and theoretical calculations. Experimental evidence for the pure Néel polar skyrmions includes: 1) Planar-view polarization mapping by HAADF-STEM; 2) out-of-plane tensile strain modulation from the strain mapping; 3) maximum in-plane ion displacement (shift X) of the skyrmion for the ultrathin sample; 4) multiple parallel "subrod" signals near the Bragg peak are clearly observed in the 3D RSM patterns. This finding is significant for the future exploration of skyrmion-based ferroelectric physics and related electronic devices. The characteristics of severely twisted domain walls vanish as the film thickness decreases, coinciding with the disappearance of Bloch features. Phase-field simulations further confirm the formation of ferroelectric Néel-skyrmion. In this scenario, the substantial reduction in Landau energy and the concomitant rise in depolarization energy are pivotal in mediating the interplay among lattice, orbital, spin, and charge degrees of freedom, thereby confining Néel-skyrmions to a 2 u.c. thick PTO layer. It should be noted that the size of the polar skyrmions observed in our system is among the smallest that have been reported so far.

4. Experimental Section

Reproducible Synthesis of Bilayers Using Pulsed-Laser Deposition (PLD): The $(\mathrm{PTO}_n/\mathrm{STO}_n)_1$ ($n = 50, 24, 14, 2$ u.c.) bilayers were deposited on (001)-$\mathrm{SrTiO_3}$ substrates using the Coherent COMPex Pro 201 F KrF excimer laser with $\lambda = 248$ nm. The $\mathrm{PbTiO_3}$ target is 3 mole percent of Pb-enriched sintered ceramics. The $\mathrm{SrTiO_3}$ target is sintered ceramics

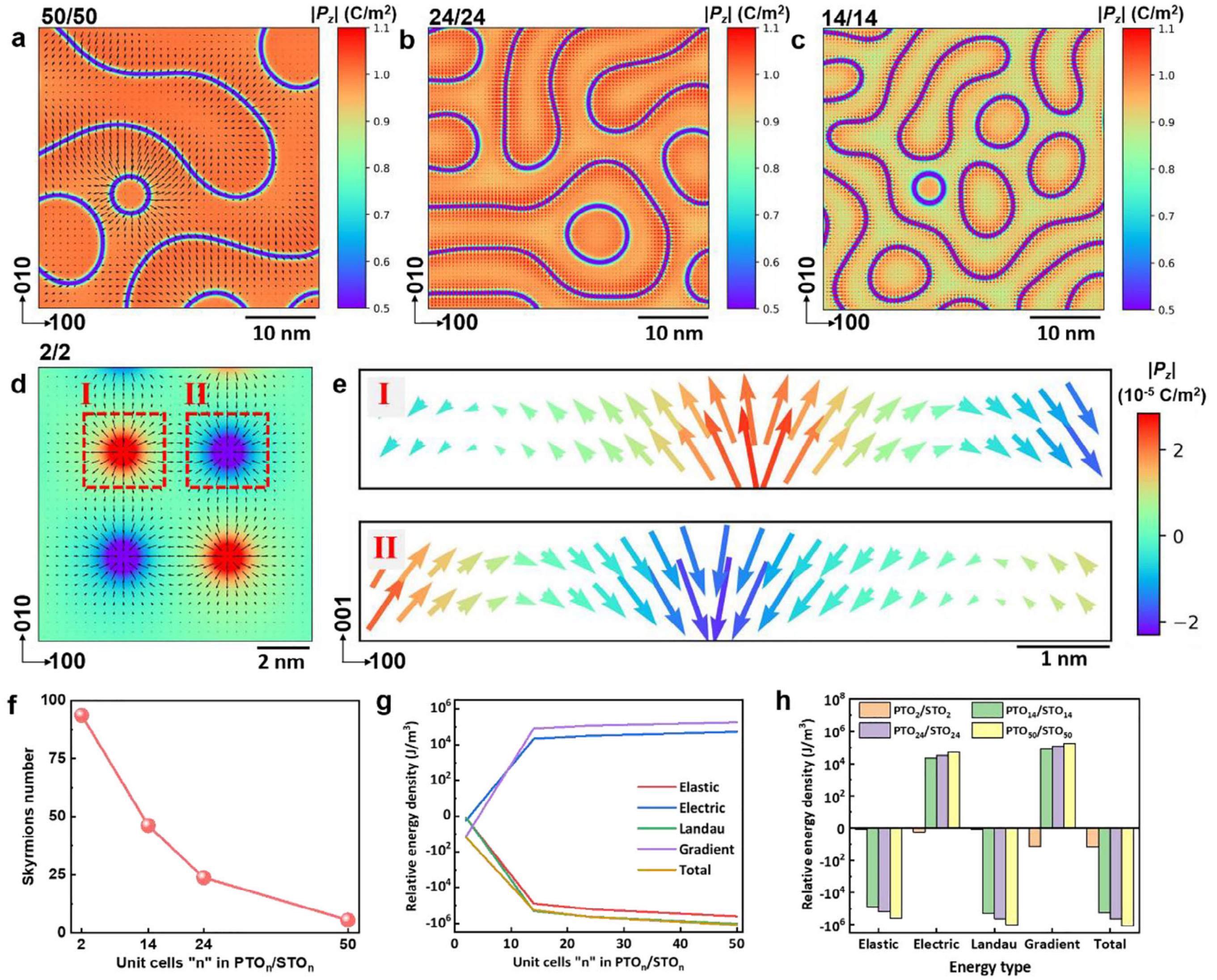

Figure 4. Thickness-dependent skyrmion-bubble to Néel-skyrmion transition simulated by the phase field method. a-d) A series of in-plane polarization distribution images for $(\mathrm{PTO}_n/\mathrm{STO}_n)_1$ ($n = 50$, 24, 14, 2 u.c.) bilayers with the out-of-plane polarization intensity. e) The cross-sectional polarization distribution vector diagram in the box of (d) I and II. f) Skyrmions number for $(\mathrm{PTO}_n/\mathrm{STO}_n)_1$ with an area of 78.4 × 78.4 nm. g,h) Relative elastic, electric, Landau, gradient, and total energy density for $(\mathrm{PTO}_n/\mathrm{STO}_n)_1$ ($n = 50$, 24, 14, 2 u.c.).

with a standard stoichiometric ratio. The growth temperature and oxygen pressure for the bilayers were 700 °C and 75 mtorr, respectively. The deposition rate is 4 Hz. By adjusting the laser energy and oxygen pressure, it could be ensured that the plasma plume reaches a height exactly 2/3 of the distance between the target and the substrate. By precisely controlling the number of pulses of lasers, the thicknesses of the $\mathrm{PbTiO_3}$ and $\mathrm{SrTiO_3}$ layers were held at 50, 24, 14, and 2 u.c., respectively. Immediately after the growth of the $(\mathrm{PTO}_n/\mathrm{STO}_n)_1$ bilayers, the samples were cooled down to room temperature under a 200 torr oxygen pressure.

Scanning Transmission Electron Microscopy (STEM): Cross-sectional samples for STEM observation were prepared by slicing, gluing, mechanical grinding, dimpling, and finally ion milling. The samples were dimpled down to 10 µm. Then, a Gatan Precision Ion Polishing System (PIPS) 695 was used for ion milling. At the beginning of ion milling, the incident angles of 7° and milling voltage of 5 kV were used. Then, the angles and voltage were gradually reduced to 3° and 3.5 kV. Finally, the ion milling voltage was set at 0.3 kV to reduce the amorphous layer produced by ion beam damage. Plan-view samples were milled only from the substrate side. The observations were performed by spherical aberration-corrected transmission electron microscopy (Titan Themis 60–300 X-FEG microscope (Thermo Fisher Scientific)), with double aberration (Cs) correctors from CEOS and a monochromator, which was operated at 300 kV. The HAADF-STEM images for acquiring the polarization distribution are recorded by Drift Corrected Frame Integration (DCFI) in Velox software. The DCFI technique records successive HAADF-STEM images and integrates a new STEM image by calculating and correcting the drift from the cross-correlation.

Structural Characterization Using Synchrotron X-Ray Diffraction: The CTR and 3D-RSMs experiment data were obtained from synchrotron X-ray diffraction. The CTR specular data were obtained by subtracting the background signal from the area detector, then applying geometry correction. The COBRA algorithm used CTR specular data to reconstruct the electron density at surfaces and interfaces in the z-direction of epitaxial films. The 3D-RSMs were employed to study the complex phase coexistence in the bilayer films. The CTR and 3D-RSMs experiments were performed at the BL02U2 beamline of the Shanghai Synchrotron Radiation Facility. The CTR specular data were collected using the spec four-circle mode. In order to amplify the surface signal as much as possible and to ensure that the incident spot does not extend beyond the surface of the sample, the 3D-RSMs experimental data were collected using spec PSI-circle fix alpha mode and a fixed incidence angle of 2 degrees. The experimental sample size is 5 × 5 mm, and the spot size is 160 × 80 um in horizontal and vertical FWHM. Highly accurate CTR and 3D-RSMs were obtained by the excellent accuracy of the Huber 6-circle diffractometer equipped with an Eiger 500 K area detector.

Peak Finding: The positions of atom columns in HAADF-STEM and iDPC images were determined on the basis of the 2D Gaussian fitting, which was carried out by using the Matlab software. For accurately distinguishing between A-site atoms and B-site atoms according to the intensity of the atomic column in the HAADF-STEM image, the brightness and contrast of images have been adjusted as a whole. The lattice spacing, the shift of Ti^{4+} (δ_{Ti}), c/a, and rotation angle were deduced.

Phase-Field Simulation: Phase-field methods are performed for the $(PTO_n/STO_n)_1$ ($n = 50, 24, 14, 2$ u.c.) bilayer oxide films on a $SrTiO_3$-(001) substrate, by solving the time-dependent Ginzburg–Landau equation:[55]

$$\frac{\partial \mathrm{P}i}{\partial \mathrm{t}} = -\mathrm{L}\frac{\delta \mathrm{F}\ (\mathrm{P}i)}{\delta \mathrm{P}i} \tag{3}$$

where t, L, $\boldsymbol{P}$ are the evolution time step, the kinetic coefficient, and the polar order parameter, respectively. The total free energy F is contributed by the volume integration of Landau (f_{Land}), elastic (f_{elas}), electrostatic (f_{elec}), and polar gradient energy densities (f_{grad}), which can be expressed:[56–58]

$$\mathrm{F}\ (\mathrm{P}i) = \int [f\mathrm{land}\ (\mathrm{P}i) + f\mathrm{elas}\ (\mathrm{Pi}, \varepsilon\mathrm{kl}) + f\mathrm{elec}\ (\mathrm{Pi}, \mathrm{Ej}) + f\mathrm{grand}\ (\mathrm{Pi}, \mathrm{j})]\, \mathrm{dV} \tag{4}$$

A series of 3D meshes of 192× 192 × 200 were established, with each grid spacing of 0.4 nm. Along the out-of-plane direction, such as the $(PTO_{24}/STO_{24})_1$, the number of grids for the substrate, bilayer oxide films, and air was set to be 30, 78, and 92, respectively. Pseudo-cubic PTO and STO correspond to the lattice parameters are set to 3.957 and 3.905 Å, respectively. A series of fixed charges were added at the domain wall to simulate the charges generated by head-to-head or tail-to-tail polarization vectors. Random noise was added with a magnitude ($<0.03\ \mu C\cdot cm^{-2}$) to simulate the initial nuclei of polarization. And sufficient step sizes were calculated to ensure that the simulated system reached steady state. In the section on the effect of PTO thicknesses and epitaxial strains for skyrmions stability, the simulations are performed for a temperature of 300 K.

Supporting Information

Supporting Information is available from the Wiley Online Library or from the author.

Acknowledgements

This work is supported by the National Natural Science Foundation of China (Nos. 52122101, 52471022, 92166104, 12275344, 12304132, 92463306, U24A2013), and Guangdong Provincial Quantum Science Strategic Initiative (no. GDZX2202001, GDZX2302001). F.H.G. acknowledges the China National Postdoctoral Program for Innovative Talents (no. BX20240245) and the China Postdoctoral Science Foundation (no. 2024M752303), Y.T.C. acknowledges the China Postdoctoral Science Foundation (no. 2023M742519), and Y.J.W. acknowledges the Youth Innovation Promotion Association CAS (no. 2021187). X.R.L. and X.L.L. acknowledge the MOST of China (no. 2022YFA1603900). Z.H. also acknowledges the Fundamental Research Funds for the Central Universities (2023QZJH13) and Natural Science Foundation of Zhejiang Province (No. LR25E020003). Z.H. and K.L. are grateful for the technical support for Nano-X from Suzhou Institute of Nano-Tech and Nano-Bionics, Chinese Academy of Sciences (SINANO).

Conflict of Interest

The authors declare no competing interests.

Author Contributions

F.-H.G., S.-S.Y., and K.L. contributed equally to this work. X.-L.M. designed the experiments. F.-H.G., Y.-L.T., Y.-L.Z., and Y.-T.C. conceived the project of interfacial characterization in oxides by using aberration-corrected STEM. S.-S.Y., X.-L.L., and X.-R.L. completed the synchrotron radiation experiment. K.L., Y.-J.W., and Z.H. conducted the phase-field simulation. F.-H.G. performed the thin-film growth and STEM characterization. All authors contributed to the discussions and manuscript preparation.

Data Availability Statement

The data that support the findings of this study are available from the corresponding author upon reasonable request.

Keywords

ferroelectric films, Néel-skyrmions, phase-field simulation, topological structures, transmission electron microscopy

Received: January 20, 2025
Revised: May 27, 2025
Published online:

---

[1] C. L. Jia, K. W. Urban, M. Alexe, D. Hesse, I. Vrejoiu, *Science* **2011**, *331*, 1420.
[2] Y. L. Tang, Y. L. Zhu, X. L. Ma, A. Y. Borisevich, A. N. Morozovska, E. A. Eliseev, W. Y. Wang, Y. J. Wang, Y. B. Xu, Z. D. Zhang, S. J. Pennycook, *Science* **2015**, *348*, 547.
[3] M. Hadjimichael, Y. Q. Li, E. Zatterin, G. A. Chahine, M. Conroy, K. Moore, E. N. O' Connell, P. Ondrejkovic, P. Marton, J. Hlinka, U. Bangert, S. Leake, P. Zubko, *Nat. Mater.* **2021**, *20*, 495.
[4] X. M. Li, C. B. Tan, C. Liu, P. Gao, Y. W. Sun, P. Chen, M. Q. Li, L. Liao, R. X. Zhu, J. B. Wang, Y. C. Zhao, L. F. Wang, Z. Xu, K. H. Liu, X. L. Zhong, J. Wang, X. D. Bai, *Proc. Natl. Acad. Sci.* **2020**, *117*, 18954.
[5] E. Gradauskaite, Q. N. Meier, N. Gray, M. F. Sarott, T. Scharsach, M. Campanini, T. Moran, A. Vogel, K. D. Cid-Ledezma, B. D. Huey, M. D. Rossell, M. Fiebig, M. Trassin, *Nat. Mater.* **2023**, *22*, 1492.
[6] Y. H. Hu, J. Y. Yang, S. Liu, *Phys. Rev. Lett.* **2024**, *133*, 046802.
[7] C. T. Nelson, B. Winchester, Y. Zhang, S. J. Kim, A. Melville, C. Adamo, C. M. Folkman, S. H. Baek, C. B. Eom, D. G. Schlom, L. Q. Chen, X. Q. Pan, *Nano Lett.* **2011**, *11*, 828.
[8] A. K. Yadav, C. T. Nelson, S. L. Hsu, Z. J. Hong, J. D. Clarkson, C. M. Schlepütz, A. R. Damodaran, P. Shafer, E. Arenholz, L. R. Dedon, D. Chen, A. Vishwanath, A. M. Minor, L. Q. Chen, J. F. Scott, L. W. Martin, R. Ramesh, *Nature* **2016**, *530*, 198.
[9] Q. Li, C. T. Nelson, S. L. Hsu, A. R. Damodaran, L. L. Li, A. K. Yadav, M. McCarter, L. W. Martin, R. Ramesh, S. V. Kalinin, *Nat. Commun.* **2017**, *8*, 1468.
[10] A. R. Damodaran, J. D. Clarkson, Z. J. Hong, H. Liu, A. K. Yadav, C. T. Nelson, S. L. Hsu, M. R. McCarter, K. D. Park, V. Kravtsov, A. Farhan, Y. Dong, Z. Cai, H. Zhou, P. Aguado-Puente, P. García-Fernández, J. Íñiguez, J. Junquera, A. Scholl, M. B. Raschke, L. Q. Chen, D. D. Fong, R. Ramesh, L. W. Martin, *Nat. Mater.* **2017**, *16*, 1003.
[11] J. Y. Kim, M. J. You, K. E. Kim, K. Y. Chu, C. H. Yang, *npj Quantum Mater.* **2019**, *4*, 29.

[12] C. B. Tan, Y. Q. Dong, Y. W. Sun, C. Liu, P. Chen, X. L. Zhong, R. X. Zhu, M. W. Liu, J. M. Zhang, J. B. Wang, K. H. Liu, X. D. Bai, D. P. Yu, X. P. Ouyang, J. Wang, P. Gao, Z. L. Luo, J. Y. Li, *Nat. Commun.* **2021**, *12*, 4620.

[13] Q. Li, V. A. Stoica, M. Paściak, Y. Zhu, Y. K. Yuan, T. N. Yang, M. R. McCarter, S. Das, A. K. Yadav, S. Park, C. Dai, H. J. Lee, Y. Ahn, S. D. Marks, S. K. Yu, C. Kadlec, T. Sato, M. C. Hoffmann, M. Chollet, M. E. Kozina, S. Nelson, D. L. Zhu, D. A. Walko, A. M. Lindenberg, P. G. Evans, L. Q. Chen, R. Ramesh, L. W. Martin, V. Gopalan, J. W. Freeland, et al., *Nature* **2021**, *592*, 376.

[14] M. F. Guo, C. Q. Guo, J. Han, S. L. Chen, S. He, T. X. Tang, Q. Li, J. Strzalka, J. Ma, D. Yi, K. Wang, B. Xu, P. Gao, H. B. Huang, L. Q. Chen, S. J. Zhang, Y. H. Lin, C. W. Nan, Y. Shen, *Science* **2021**, *371*, 1050.

[15] D. Rusu, J. J. P. Peters, T. P. A. Hase, J. A. Gott, G. A. A. Nisbet, J. Strempfer, D. Haskel, S. D. Seddon, R. Beanland, A. M. Sanchez, M. Alexe, *Nature* **2022**, *602*, 240.

[16] P. Behera, M. A. May, F. Gómez-Ortiz, S. Susarla, S. Das, C. T. Nelson, L. Caretta, S. L. Hsu, M. R. McCarter, B. H. Savitzky, E. S. Barnard, A. Raja, Z. J. Hong, P. García-Fernandez, S. W. Lovesey, G. van der Laan, P. Ercius, C. Ophus, L. W. Martin, J. Junquera, M. B. Raschke, R. Ramesh, *Sci. Adv.* **2022**, *8*, abj8030.

[17] V. Govinden, P. R. Tong, X. W. Guo, Q. Zhang, S. Mantri, M. M. Seyfouri, S. Prokhorenko, Y. Nahas, Y. J. Wu, L. Bellaiche, T. L. Sun, H. Tian, Z. J. Hong, N. Valanoor, D. Sando, *Nat. Commun.* **2023**, *14*, 4178.

[18] G. Sánchez-Santolino, V. Rouco, S. Puebla, H. Aramberri, V. Zamora, M. Cabero, F. A. Cuellar, C. Munuera, F. Mompean, M. Garcia-Hernandez, A. Castellanos-Gomez, J. Íñiguez, C. Leon, J. Santamaria, *Nature* **2024**, *626*, 529.

[19] C. Jeong, J. Lee, H. Jo, J. Oh, H. Baik, K. J. Go, J. Son, S. Y. Choi, S. Prosandeev, L. Bellaiche, Y. Yang, *Nat. Commun.* **2024**, *15*, 3887.

[20] F. F. Xin, L. Falsi, Y. Gelkop, D. Pierangeli, G. Q. Zhang, F. Bo, F. Fusella, A. J. Agranat, E. DelRe, *Phys. Rev. Lett.* **2024**, *132*, 066603.

[21] Z. W. Li, Y. J. Wang, G. Tian, P. L. Li, L. N. Zhao, F. Y. Zhang, J. X. Yao, H. Fan, X. Song, D. Y. Chen, Z. Fan, M. H. Qin, M. Zeng, Z. Zhang, X. B. Lu, S. J. Hu, C. H. Lei, Q. F. Zhu, J. Y. Li, X. S. Gao, J. M. Liu, *Sci. Adv.* **2017**, *3*, 1700919.

[22] J. Ma, J. Ma, Q. H. Zhang, R. C. Peng, J. Wang, C. Liu, M. Wang, N. Li, M. F. Chen, X. X. Cheng, P. Gao, L. Gu, L. Q. Chen, P. Yu, J. X. Zhang, C. W. Nan, *Nat. Nanotech.* **2018**, *13*, 947.

[23] Y. J. Wang, Y. P. Feng, Y. L. Zhu, Y. L. Tang, L. X. Yang, M. J. Zou, M. J. Han, X. W. Guo, B. Wu, X. L. Ma, *Nat. Mater.* **2020**, *19*, 881.

[24] Y. Nahas, S. Prokhorenko, J. Fischer, B. Xu, C. Carrétéro, S. Prosandeev, M. Bibes, S. Fusil, B. Dkhil, V. Garcia, L. Bellaiche, *Nature* **2020**, *577*, 47.

[25] Y. Nahas, S. Prokhorenko, L. Louis, Z. Gui, I. Kornev, L. Bellaiche, *Nat. Commun.* **2015**, *6*, 8542.

[26] S. Das, Y. L. Tang, Z. J. Hong, M. A. P. Gonçalves, M. R. McCarter, C. Klewe, K. X. Nguyen, F. Gómez-Ortiz, P. Shafer, E. Arenholz, V. A. Stoica, S. L. Hsu, B. Wang, C. Ophus, J. F. Liu, C. T. Nelson, S. Saremi, B. Prasad, A. B. Mei, D. G. Schlom, J. Íñiguez, P. García-Fernández, D. A. Muller, L. Q. Chen, J. Junquera, L. W. Martin, R. Ramesh, *Nature* **2019**, *568*, 368.

[27] P. Zubko, *Nature* **2019**, *568*, 322.

[28] S. Das, Z. J. Hong, V. A. Stoica, M. A. P. Gonçalves, Y. T. Shao, E. Parsonnet, E. J. Marksz, S. Saremi, M. R. McCarter, A. Reynoso, C. J. Long, A. M. Hagerstrom, D. Meyers, V. Ravi, B. Prasad, H. Zhou, Z. Zhang, H. Wen, F. Gómez-Ortiz, P. García-Fernández, J. Bokor, J. Íñiguez, J. W. Freeland, N. D. Orloff, J. Junquera, L. Q. Chen, S. Salahuddin, D. A. Muller, L. W. Martin, R. Ramesh, *Nat. Mater.* **2021**, *20*, 194.

[29] J. Yin, H. X. Zong, H. Tao, X. F. Tao, H. J. Wu, Y. Zhang, L. D. Zhao, X. D. Ding, J. Sun, J. G. Zhu, J. G. Wu, S. J. Pennycook, *Nat. Commun.* **2021**, *12*, 3632.

[30] L. M. Zhou, Y. H. Huang, S. Das, Y. L. Tang, C. Li, H. Tian, L. Q. Chen, Y. J. Wu, R. Ramesh, Z. J. Hong, *Matter* **2022**, *5*, 1031.

[31] L. Han, C. Addiego, S. Prokhorenko, M. Y. Wang, H. Y. Fu, Y. Nahas, X. X. Yan, S. H. Cai, T. Q. Wei, Y. H. Fang, H. Z. Liu, D. X. Ji, W. Guo, Z. B. Gu, Y. R. Yang, P. Wang, L. Bellaiche, Y. F. Chen, D. Wu, Y. F. Nie, X. Q. Pan, *Nature* **2022**, *603*, 63.

[32] R. X. Zhu, Z. X. Jiang, X. X. Zhang, X. L. Zhong, C. B. Tan, M. W. Liu, Y. W. Sun, X. M. Li, R. S. Qi, K. Qu, Z. T. Liu, M. Wu, M. Q. Li, B. Y. Huang, Z. Xu, J. B. Wang, K. H. Liu, P. Gao, J. Wang, J. Y. Li, X. D. Bai, *Phys. Rev. Lett.* **2022**, *129*, 107601.

[33] Y. T. Shao, S. Das, Z. J. Hong, R. J. Xu, S. Chandrika, F. Gómez-Ortiz, P. García-Fernández, L. Q. Chen, H. Y. Hwang, J. Junquera, L. W. Martin, R. Ramesh, D. A. Muller, *Nat. Commun.* **2023**, *14*, 1355.

[34] F. H. Gong, Y. L. Tang, Y. J. Wang, Y. T. Chen, B. Wu, L. X. Yang, Y. L. Zhu, X. L. Ma, *Nat. Commun.* **2023**, *14*, 3376.

[35] S. Yuan, Z. H. Chen, S. Prokhorenko, Y. Nahas, L. Bellaiche, C. H. Liu, B. Xu, L. Cheng, S. Das, L. W. Martin, *Phys. Rev. Lett.* **2023**, *130*, 226801.

[36] S. X. Wang, W. Li, C. G. Deng, Z. J. Hong, H. B. Gao, X. L. Li, Y. L. Gu, Q. Zheng, Y. J. Wu, P. G. Evans, J. F. Li, C. W. Nan, Q. Li, *Nat. Commun.* **2024**, *15*, 1374.

[37] L. Y. Gao, S. Prokhorenko, Y. Nahas, L. Bellaiche, *Phys. Rev. Lett.* **2024**, *132*, 026902.

[38] H. X. Shang, H. T. Dong, Y. H. Wu, F. Deng, X. Liang, S. L. Hu, S. P. Shen, *Phys. Rev. Lett.* **2024**, *132*, 116201.

[39] V. Govinden, S. Prokhorenko, Q. Zhang, S. Rijal, Y. Nahas, L. Bellaiche, N. Valanoor, *Nat. Mater.* **2023**, *22*, 553.

[40] P. Shafer, P. García-Fernández, P. Aguado-Puente, A. R. Damodaran, A. K. Yadav, C. T. Nelson, S. L. Hsu, J. C. Wojdeł, J. Íñiguez, L. W. Martin, E. Arenholz, J. Junquera, R. Ramesh, *Proc. Natl. Acad. Sci* **2018**, *115*, 915.

[41] P. Zubko, J. C. Wojdeł, M. Hadjimichael, S. Fernandez-Pena, A. Sené, I. Luk'yanchuk, J. M. Triscone, J. Íñiguez, *Nature* **2016**, *534*, 524.

[42] A. K. Yadav, K. X. Nguyen, Z. J. Hong, P. García-Fernández, P. Aguado-Puente, C. T. Nelson, S. Das, B. Prasad, D. Kwon, S. Cheema, A. I. Khan, C. M. Hu, J. Íñiguez, J. Junquera, L. Q. Chen, D. A. Muller, R. Ramesh, S. Salahuddin, *Nature* **2019**, *565*, 468.

[43] H. S. Kum, H. Lee, S. Kim, S. Lindemann, W. Kong, K. Qiao, P. Chen, J. Irwin, J. H. Lee, S. Xie, S. Subramanian, J. Shim, S. H. Bae, C. Choi, L. Ranno, S. Seo, S. Lee, J. Bauer, H. S. Li, K. Lee, J. A. Robinson, C. A. Ross, D. G. Schlom, M. S. Rzchowski, C. B. Eom, J. Kim, *Nature* **2020**, *578*, 75.

[44] B. Gobel, I. Mertig, O. A. Tretiakov, *Phys. Rep.* **2021**, *895*, 1.

[45] B. Gobel, J. Henk, I. Mertig, *Sci. Rep* **2019**, *9*, 9521.

[46] X. Z. Yu, M. Mostovoy, Y. Tokunaga, W. Z. Zhang, K. Kimoto, Y. Matsui, Y. Kaneko, N. Nagaosa, Y. Tokura, *Proc. Natl. Acad. Sci* **2012**, *109*, 8856.

[47] M. A. Pereira Gonçalves, C. Escorihuela-Sayalero, P. Garca-Fernández, J. Junquera, J. Íñiguez, *Sci. Adv.* **2019**, *5*, aau7023.

[48] J. Hlinka, P. Ondrejkovic, *Solid State Phys* **2019**, *90*, 143.

[49] J. H. Ren, L. J. Liu, F. Sun, Q. He, M. J. Wu, W. J. Chen, Y. Zheng, *Acta Mater.* **2024**, *276*, 120154.

[50] Y. Yacoby, M. Sowwan, E. Stern, J. O. Cross, D. Brewe, R. Pindak, J. Pitney, E. M. Dufresne, R. Clarke, *Nat. Mater.* **2002**, *1*, 99.

[51] Y. Wakabayashi, J. Takeya, T. Kimura, *Phys. Rev. Lett.* **2010**, *104*, 066103.

[52] Y. K. Yuan, Y. F. Lu, G. Stone, K. Wang, C. M. Brooks, D. G. Schlom, S. B. Sinnott, H. Zhou, V. Gopalan, *Nat. Commun.* **2018**, *9*, 5220.

[53] S. C. Abrahams, S. K. Kurtz, P. B. Jamieson, *Phys. Rev.* **1968**, *172*, 551.

[54] W. Zhong, R. D. King-Smith, D. Vanderbilt, *Phys. Rev. Lett.* **1994**, *72*, 3618.

[55] L. Q. Chen, *J. Am. Ceram. Soc.* **2008**, *91*, 1835.

[56] Y. L. Li, S. Y. Hu, Z. K. Liu, L. Q. Chen, *Acta Mater.* **2002**, *50*, 395.

[57] Y. L. Li, S. Y. Hu, Z. K. Liu, L. Q. Chen, *Appl. Phys. Lett.* **2002**, *81*, 427.

[58] Z. J. Hong, A. R. Damodaran, F. Xue, S. L. Hsu, J. Britson, A. K. Yadav, C. T. Nelson, J. J. Wang, J. F. Scott, L. M. Martin, R. Ramesh, L. Q. Chen, *Nano Lett.* **2017**, *17*, 2246.